Quaternary Science Reviews 248 (2020) 106602

Contents lists available at ScienceDirect

Quaternary Science Reviews

journal homepage: www.elsevier.com/locate/quascirev

Paleoenvironments from robust loess stratigraphy using high-resolution color and grain-size data of the last glacial Krems-Wachtberg record (NE Austria)

Tobias Sprafke [a, *], Philipp Schulte [b], Simon Meyer-Heintze [c], Marc Händel [d], Thomas Einwögerer [d], Ulrich Simon [d], Robert Peticzka [e], Christian Schäfer [c], Frank Lehmkuhl [b], Birgit Terhorst [c]

[a] Institute of Geography, University of Bern, Hallerstrasse 12, 3012, Bern, Switzerland
[b] Department of Geography, RWTH Aachen University, Wüllnerstr. 5b, 52056, Aachen, Germany
[c] Institute of Geography and Geology, University of Würzburg, Am Hubland, 97074, Würzburg, Germany
[d] Institute for Oriental and European Archaeology, Austrian Academy of Sciences, Hollandstraße 11-13, 1020, Vienna, Austria
[e] Department of Geography and Regional Research, University of Vienna, Althanstraße 14, 1090, Vienna, Austria

ARTICLE INFO

Article history:
Received 3 April 2020
Received in revised form
5 September 2020
Accepted 12 September 2020
Available online 1 October 2020

Keywords:
Loess
Paleosol
Spectrophotometry
Granulometry
Paleoenvironment
Paleoclimate
Alpine foreland
Last Glacial Maximum
Late Pleistocene
Upper Paleolithic

ABSTRACT

The complex interplay of dust sedimentation, pedogenesis, and erosion/reworking in the formation of loess-paleosol sequences (LPS) challenges paleoenvironmental proxies. Here we show that color and grain size are essential parameters characterizing loess profiles and support robust stratigraphies as a basis for reconstructions in the context of local geo-ecological and large-scale paleoclimatic evolution. Detailed paleoenvironmental records from the period since the arrival of anatomically modern humans to the last glacial maximum are scarce in the Alpine surroundings. The c. 7.5 m thick LPS Krems-Wachtberg, NE Austria, known for its well-preserved Upper Paleolithic context at a depth of 5.5 m, formed between 40 and 20 ka BP by quasi-continuous dust-sedimentation, interrupted by phases of incipient pedogenesis and local reworking. The new KW2015 composite is based on three sections studied and sampled at 2.5 cm resolution. Color and grain size data support a robust stratigraphy for reconstructions of the pedosedimentary evolution. The marked transition from oxidized to reduced paleosols of KW2015 around 34–35 ka corresponds to the Middle-to Upper Pleniglacial transition as part of a general cooling trend from marine isotope stage (MIS) 3 to 2, intensely modulated by millennial-scale climatic fluctuations as recorded in the Greenland ice core data. The distinct response of KW2015 to these trends highlights that reconstructing LPS evolution based on a robust stratigraphy is a prerequisite to paleoenvironmental proxy interpretation.

Author statement

Tobias Sprafke: Conceptualization, Methodology, Formal analysis, Investigation, Writing - original draft, Visualization. Philipp Schulte: Methodology, Formal analysis, Investigation, Writing - review & editing, Visualization. Simon Meyer-Heintze: Methodology, Investigation, Writing - review & editing. Marc Händel: Resources, Writing - review & editing. Thomas Einwögerer: Resources, Funding acquisition. Ulrich Simon: Resources, Writing - review & editing. Robert Peticzka: Resources, Supervision. Christian Schäfer: Methodology, Writing - review & editing. Frank Lehmkuhl: Resources, Writing - review & editing, Supervision, Funding acquisition. Birgit Terhorst: Resources, Supervision, Writing - review & editing

1. Introduction

Loess-paleosol sequences (LPS) record local geo-ecological responses to climatic shifts and are widespread in areas of past and present human settlement in Europe (Fitzsimmons et al., 2012; Lehmkuhl et al., 2016). Recent years have seen fundamental advances related to proxies and chronologies from LPS (Thiel et al.,

* Corresponding author.
E-mail address: tobias.sprafke@giub.unibe.ch (T. Sprafke).

https://doi.org/10.1016/j.quascirev.2020.106602

2011; Zech et al., 2013; Häggi et al., 2014; Prud'homme et al., 2016; Moine et al., 2017). Current LPS research relies mainly on multi-method approaches, quantifying e.g. grain sizes (GS), magnetic susceptibility (MS), (bio)geochemistry or color (Gocke et al., 2014; Lukić et al., 2014; Krauss et al., 2016; Fischer et al., 2019).

Comparably few studies provide detailed stratigraphic information and evaluate the formation processes of LPS, which is prerequisite to interpreting their parameter variations (Antoine et al., 2013; Meszner et al., 2013; Sprafke, 2016; Meyer-Heintze et al., 2018). Pedogenic processes overprint loess during phases of absent or low sedimentation and reflect ecological conditions. The tight chronology for the last glacial reference LPS Nussloch (Moine et al., 2017) demonstrates strong links between millennial climatic events and paleosol types/intensities in Central European LPS (Rousseau et al., 2017a). However, interpretations of LPS can be complicated by reworking and erosion events (Lehmkuhl et al., 2016; Sprafke, 2016).

Depending on the scientific background of researchers, stratigraphic descriptions of LPS strongly differ in detail and unit designation; the unified nomenclature set by the former INQUA subcommission of loess stratigraphy in the 1960s (Fink, 1965, 1969) has been abandoned. Soil horizon designations appear reasonable for loess stratigraphy as pedogenic pigmentation causes most visible variations in LPS (Bronger, 1976, 2008; Schirmer, 2000, 2016; Sprafke, 2016). Spectrophotometers quantify color variations of LPS and enhance the robustness and detail of stratigraphic logs derived from field descriptions (Sprafke, 2016). Here, we argue that a combination of this approach with detailed granulometry (Vandenberghe, 2013; Schulte et al., 2018) captures the main forming processes of LPS in the interplay of dust deposition, pedogenesis and local reworking, bridging the gap to proxy interpretation.

In the Alps and their forelands only few paleoclimate records are available for the timespan since the arrival of anatomically modern humans (AMH; c. 43.5 ka) and the end of the Last Glacial Maximum (LGM; c. 20 ka) (Heiri et al., 2014; Nigst et al., 2014; Mayr et al., 2019; Stojakowits et al., in press). During this period, the c. 7.5 m thick LPS Krems-Wachtberg (NE Austria) formed by more or less continuous dust accumulation, interrupted by phases of incipient pedogenesis and reworking (Hambach et al., 2008; Einwögerer et al., 2014; Händel et al., 2014; Lomax et al., 2014). Different parts of the section were exposed during archeological excavations that lasted from 2005 until 2015 (Händel et al., 2014; Händel, 2017). In total seven archeological find horizons (AH) are reported, of which the Gravettian (Mid Upper Paleolithic) AH 4 at c. 5.5 m depth provided the vast majority of findings, including part of an occupation layer with infant burials and hearths dated to c. 31 ka cal BP (Einwögerer et al., 2006; Brandl et al., 2014; Fladerer et al., 2014; Händel et al., 2014; Simon et al., 2014).

The LPS Krems-Wachtberg is located in a (paleo-)geographical bridge position from Central-to SE-Europe (Fig. 1) and provides high-resolution paleoenvironmental information for the transition from the milder Marine Isotope Stage (MIS) 3 to MIS 2, corresponding roughly to the Middle- (MPG) to Upper Pleniglacial (UPG; Moine et al., 2017; Zens et al., 2018). High-resolution MS data (Hambach, 2010; Groza et al., 2019) and a horizon-wise study of the upper 6 m (Terhorst et al., 2014) did not unravel the complex evolution of the complete section. Before the Krems-Wachtberg excavation was backfilled for house construction in 2015, the entire LPS was accessible in three complementary profiles (KW-A, -B, −C). This paper presents a detailed revised stratigraphy of the LPS Krems-Wachtberg (KW2015 composite) that combines field documentation with high-resolution color and GS data. The reconstruction of the local interplay of dust deposition, pedogenesis and reworking provides semi-quantitative paleoenvironmental information, which is discussed in the context of the Central European MPG/UPG paleoclimatic evolution. This study highlights that complex terrestrial archives like LPS require a detailed stratigraphic analysis involving the reconstruction of their forming processes before parameter variations along vertical sections are interpreted as paleoclimatic and -environmental proxies.

2. Study site

For more than 100 years, the thick loess cover at Krems a. d. Donau (NE Austria) has attracted both loess researchers and archeologists (Penck, 1903; Fink, 1976; Fink and Kukla, 1977; Einwögerer et al., 2014; Händel et al., 2014; Sprafke, 2016; Händel, 2017). The c. 7.5 m thick LPS Krems-Wachtberg is located at 250 m a.s.l. on a slightly SE-inclined plateau 50 m above present day Danube level on a spur created by the incision of the Danube and Krems River into crystalline rocks of the Bohemian Massif (Fig. 1; Fuchs and Grill, 1984). Weathered Neogene to Pleistocene fluvial sediments are overlain by loess packages of up to 37 m thickness, depending on paleotopography (Einwögerer et al., 2014; Sprafke, 2016). At Krems-Schießstätte loess reaches back to the Early Pleistocene Olduvai magnetic chron (Fink and Kukla, 1977). The SE tip of the spur is a strategic panorama position used since the Early

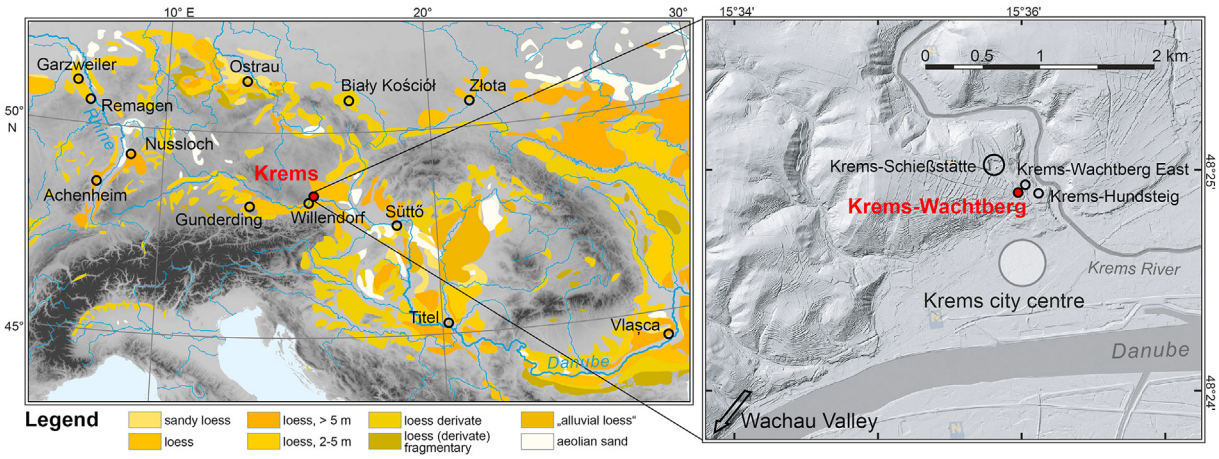

Fig. 1. Position of Krems-Wachtberg with neighboring profiles and other well-resolved last glacial loess profiles within the European loess belt including sites used to calculate a European Average Loess (EAL_19, see Fig. 7) (loess map adapted from Haase et al., 2007, Sprafke, 2016, local topography from NÖ Atlas, 2015).

Upper Paleolithic, as witnessed by a number of archeological find layers in the youngest loess. The Wachtberg area has recently gained attraction as residential area, resulting in the abandonment of old vineyards and numerous prospections, core drillings, rescue excavations, and two long term archeological campaigns at Krems-Hundsteig (2000–2002) and Krems-Wachtberg (2005–2015) (Neugebauer-Maresch, 2008; Einwögerer et al., 2014; Neugebauer-Maresch et al., 2014; Händel, 2017).

2.1. Previous profiles and general stratigraphy

Händel et al. (2014) summarize the history of the Krems-Wachtberg excavation and give an overview of the main loess profiles (Fig. 2), which are all characterized by a similar stratigraphy with very little lateral variation. Several local marker horizons in the weakly differentiated loess sediments have supported a stratigraphic framework for the whole excavation, with layers slightly dipping southeast (Händel et al., 2014). 39 macroscopically identifiable geological horizons (GH) were labelled in 2005 from the topsoil to the gravel/rock at the bottom (GH 39). GH 5 to GH 38 are yellowish to slightly brownish and partly greyish/grey loess sediments. Some units with a higher amount of coarse material from upslope (weathered crystalline rock and fluvial deposits) and partly sharp boundaries result from reworking/erosion (Händel et al., 2014; Heiri et al., 2014; Terhorst et al., 2014).

All samples taken from various researchers during the ten years of exposure are documented in the excavation database; most are displayed in the profile sketches of Händel et al. (2014). High-resolution data of MS (Hambach, 2010) and numerous luminescence ages (Lomax et al., 2014) derive from an almost 8 m thick section at North Profile 2005–6 (Fig. 2A–D). The South Profile 2005–7/10–11 on the opposite site of the excavation was very close to the double infant burial (Fig. 2B; Einwögerer et al., 2006), but did not expose the lower 2 m of the LPS (Händel et al., 2014). From this profile, Terhorst et al. (2014) published field descriptions and results of sedimentological and geochemical analyses from each visible GH. In the two deep trenches to the bedrock that were dug in 2009 and 2013/2014 (Fig. 2E+F), the horizons beneath GH 28 were labelled GH 50–62 (61 = gravel, 62 = bedrock) in sounding DE98-100 (West Profile, 2009–11) and GH 80–90 (89 = gravel, 90 = bedrock) in sounding AB94-95 accessible to us in autumn 2013, which was extended by 1 m to both east and north in 2014 (sounding A-C94-96).

2.2. Geochronological framework

All published ages from the 2005–2015 Krems-Wachtberg excavation are shown in Fig. 3, using the compilation from the supplement of Heiri et al. (2014), complemented by luminescence ages from Groza et al. (2019) and the radiocarbon age of the mammoth scapula covering the double infant burial (Händel, 2017). The high-resolution environmental magnetic study of Hambach et al. (2008) was the first paleoenvironmental and chronological interpretation for the whole LPS Krems-Wachtberg and was adopted by Terhorst et al. (2014). The MS age model (Fig. 3, cf. Heiri et al., 2014) is based on the assumption that phases of enhanced

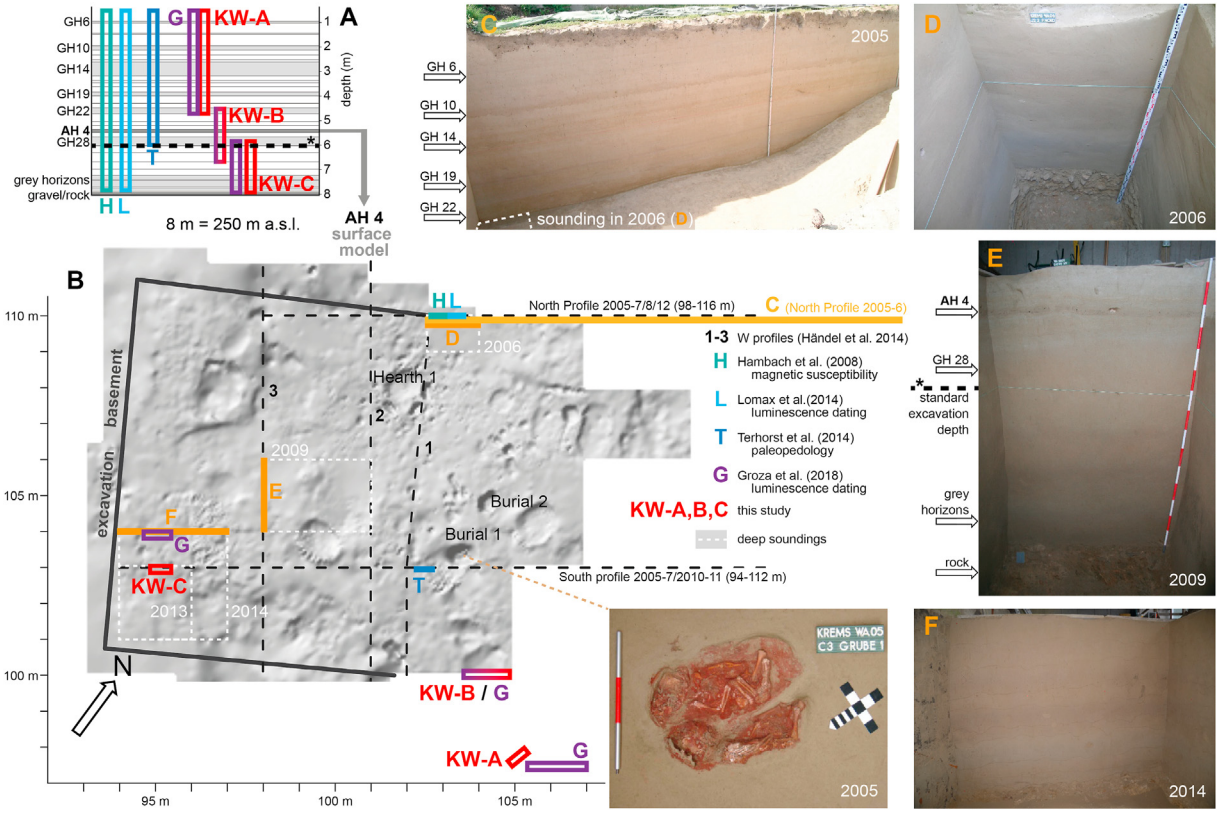

Fig. 2. The LPS at the archeological excavation Krems-Wachtberg 2005–2015 with selected geological horizons (GH) defined during the excavation for reference. A: Generalized stratigraphic scheme of the LPS and stratigraphic relation profiles KW-A, -B, –C (this study) to the profiles studied by Hambach et al. (2010), Lomax et al. (2014), Terhorst et al. (2014), and Groza et al. (2019), marked H, L, T, and G, respectively. B: Surface model of main occupation horizon AH 4 including the location of infant burials (Einwögerer et al., 2006) and the multiphased hearth 1; main profile walls from Händel et al. (2014). Locations of vertical sections (see 2A) and deep soundings with year of exposure. C: North profile in 2005 with prominent GH marked. D: Deep sounding at North profile 2005–6; E: Deep sounding from 2009 with prominent features marked. F: Deep sounding from 2014 expanded from the sounding in 2013 sampled for this study (KW–C in Fig. 4).

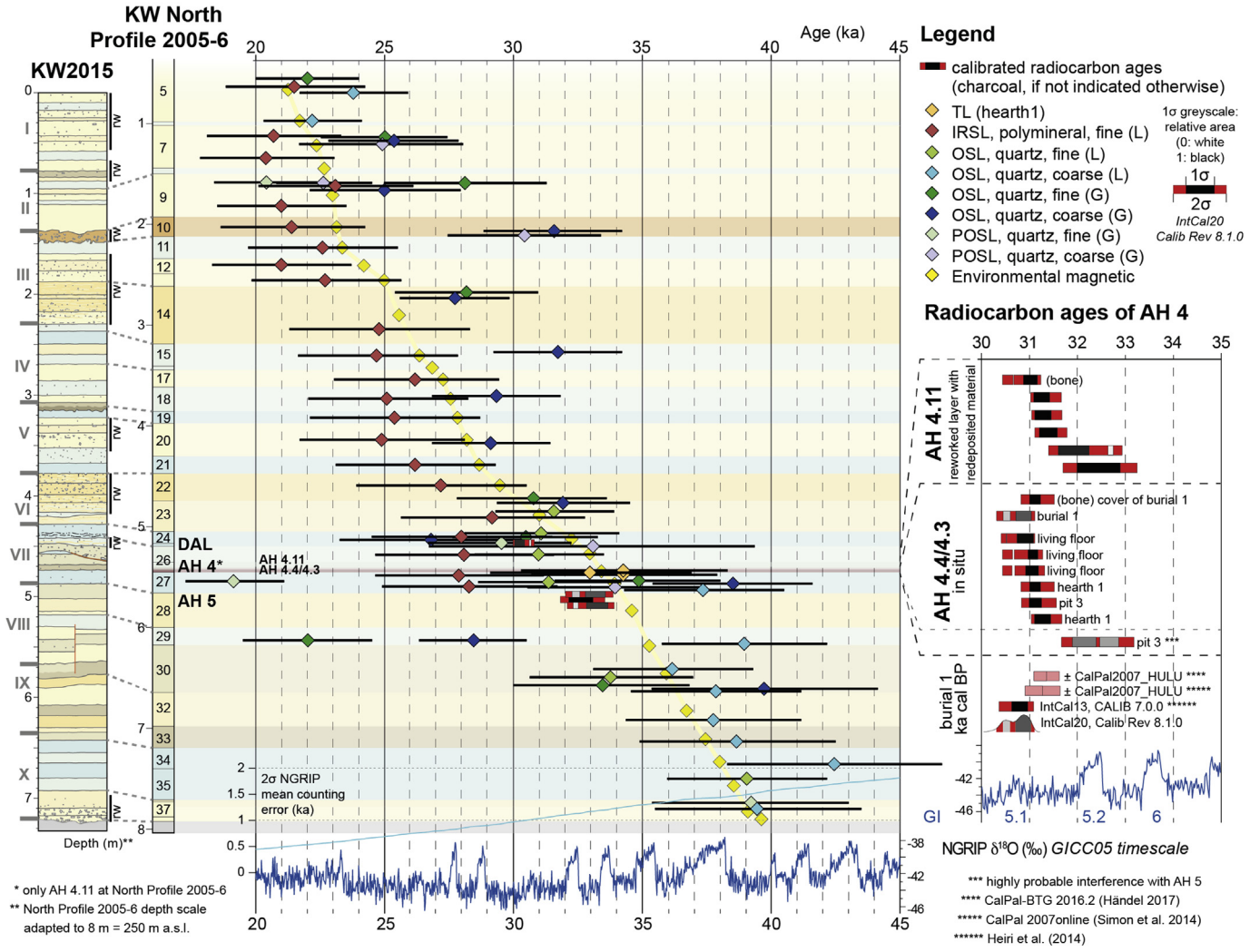

Fig. 3. Geochronological information from the LPS Krems-Wachtberg related to the stratigraphy of North Profile 2005–6 and comparison with the KW2015 composite (Fig. 8). Horizontal age axis shows NGRIP $\delta^{18}O$ variations including counting error for comparison (Rasmussen et al., 2006, 2014). Radiocarbon ages from Händel (2017) calibrated with Calib 8.1.0 (Stuiver and Reimer, 1993) using the IntCal20 calibration curve (Reimer et al., 2020), with close up of ages from AH 4 compared to the NGRIP $\delta^{18}O$ variations with GI marked. The example of the youngest AH 4 radiocarbon age from charcoal in the infant burial illustrates possible offsets related to different calibrations (section 2.2). TL ages of baked loess from beneath hearth1 by Zöller et al. (2014). Luminescence ages from Lomax et al. (2014) and Groza et al. (2019) marked by (L) and (G), respectively, in the legend. Environmental magnetic age model by Hambach (2010) shown for comparison (cf. Heiri et al., 2014).

pedogenesis detected by environmental magnetism are connected to a more humid/warmer climate, allowing correlations to higher $\delta^{18}O$ values (Greenland Interstadials [GI]) of the chronologically robust NGRIP ice core record (Hambach, 2010; Rasmussen et al., 2014). Relative paleointensity variations traced by paleomagnetic analyses indicate a formation of AH 4 contemporary to the Mono Lake event around 34.2 ± 1.2 ka (Hambach et al., 2008; Laj et al., 2014). This estimate agrees with three thermoluminescence (TL) ages of "baked loess" directly below hearth 1, with a weighted mean of 33.9 ± 2.3 ka (Zöller et al., 2014).

A set of 38 luminescence ages from North Profile 2005-6 spans the whole LPS and indicates more or less continuous sedimentation between 40 and 20 ka and no major hiatus; smaller gaps cannot be identified due to relatively large errors (Lomax et al., 2014). Three luminescence laboratories contributed with different approaches to certain parts of the record, whereby Groza et al. (2019) analyzed 16 additional samples from the whole sequence; however, due to their scatter, the obtained ages did not lead to a more precise chronostratigraphy (Fig. 3).

Radiocarbon ages with smaller errors and higher confidence are restricted to datable material. Händel (2017) compiled 44 radiocarbon ages (41 from charcoal, 3 from bone) from Krems-Wachtberg and Krems-Hundsteig to determine the main Upper Paleolithic occupation periods and phases of local reworking within this episode. All 19 radiocarbon ages from the recent Krems-Wachtberg excavation calibrated with Calib Rev 8.1.0 (Stuiver and Reimer, 1993) using the IntCal20 calibration curve (Reimer et al., 2020) are shown in Fig. 3. Charcoals from AH 5 in GH 28 yielded ages from 32.0 to 33.5 ka cal BP. Two age clusters for AH 4 in GH 26 partly overlap within the 2σ-error. Most ages from the AH 4.4/4.3 (in situ) group around 30.5 to 31.5 ka cal BP and are therefore 1–3 ka younger than dates by alternative methods (Hambach, 2010; Zöller et al., 2014). Radiocarbon ages for AH 4.11 span the timeframe of both AH 4.4/4.3 and 5, and thus confirm its stratigraphic and archeological interpretation as a layer created by slope processes that includes material from earlier Gravettian occupations (Händel, 2017). This layer is sealed by GH 25, identified as double ash layer (DAL) of two subsequent steppe fires and dated to 30.1–30.7 ka cal

BP (1σ).

Radiocarbon ages calibrated with CalPal-Beyond the Ghost, Version 2016.2 using the CalPal-2007-Hulu reference (Weninger and Jöris, 2008) place AH 4.4/4.3 into the stadial between GI 5.1 and 5.2, which is supported by the absence of pedological features in GH 26 (Händel, 2017). IntCal20 ages are few hundred years younger, reaching partly GI 5.1. Taking into account age errors, calibration insecurities, and a NGRIP 2σ counting error of 1 ka during this period (Fig. 3; Rasmussen et al., 2006) we follow the stratigraphic reasoning by Händel (2017).

3. Methods

3.1. Profiles and sampling

The stratigraphies along different outcrop walls at Krems-Wachtberg are macroscopically similar (Händel et al., 2014). In autumn 2013, we created three complementary profiles of the LPS few meters distant from each other (KW-A, -B, −C) as parts of the new composite profile KW2015 (Fig. 2A+B, Fig. 4). KW-A is 4 m thick and reaches from GH 5 into GH 22. Profile KW-B is 2.2 m thick, embraces AH 4 and contains the sequence of GH 21 to GH 30. KW-C

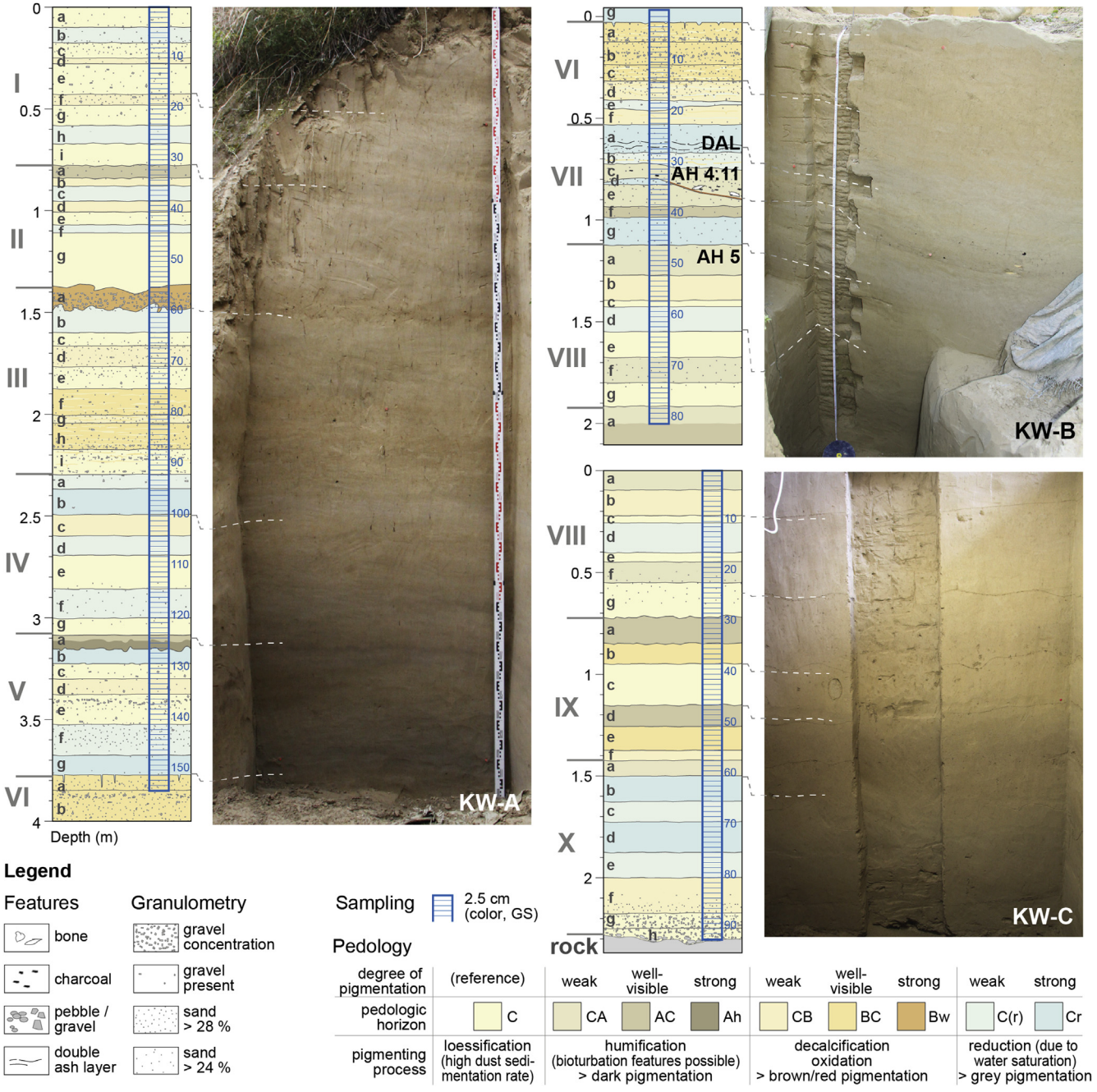

Fig. 4. Photos and profile sketch of the three studied sections KW-A, -B, −C with units, archeological horizons (AH 4.11, AH 5), double ash layer (DAL) and sampling positions. Legend adapted from Sprafke (2016) complemented by a key to the main pigmenting processes. Note that pedological horizons do not necessarily reflect in situ pigmentation by soil formation, but soil may be reworked by slope processes.

in the excavation basement is 2.4 m thick and encompasses the section from GH 28/80 down to the bedrock (GH 39/90) (Figs. 2F and 4). New MS data from sampling positions close to our three profiles were published by Groza et al. (2019) and are similar to data from North profile 2005–6 (Hambach et al., 2008). This indicates that the 7.2 m thick composite KW2015 is representative for the entire Krems-Wachtberg excavation.

Before sampling, the three profiles were thoroughly cleaned and documented following FAO (2006). Detailed field descriptions are refined by colorimetric (Fig. 5) and granulometric (Fig. 6) data measured on samples taken continuously in 2.5 cm resolution (continuous column sampling [CCS] after Antoine et al., 2009). All 312 samples (positions in Fig. 4) were air dried, sieved to fine earth size (<2 mm) and homogenized for further analyses.

3.2. Laser-granulometry

Granulometric data obtained at high resolution from LPS are a

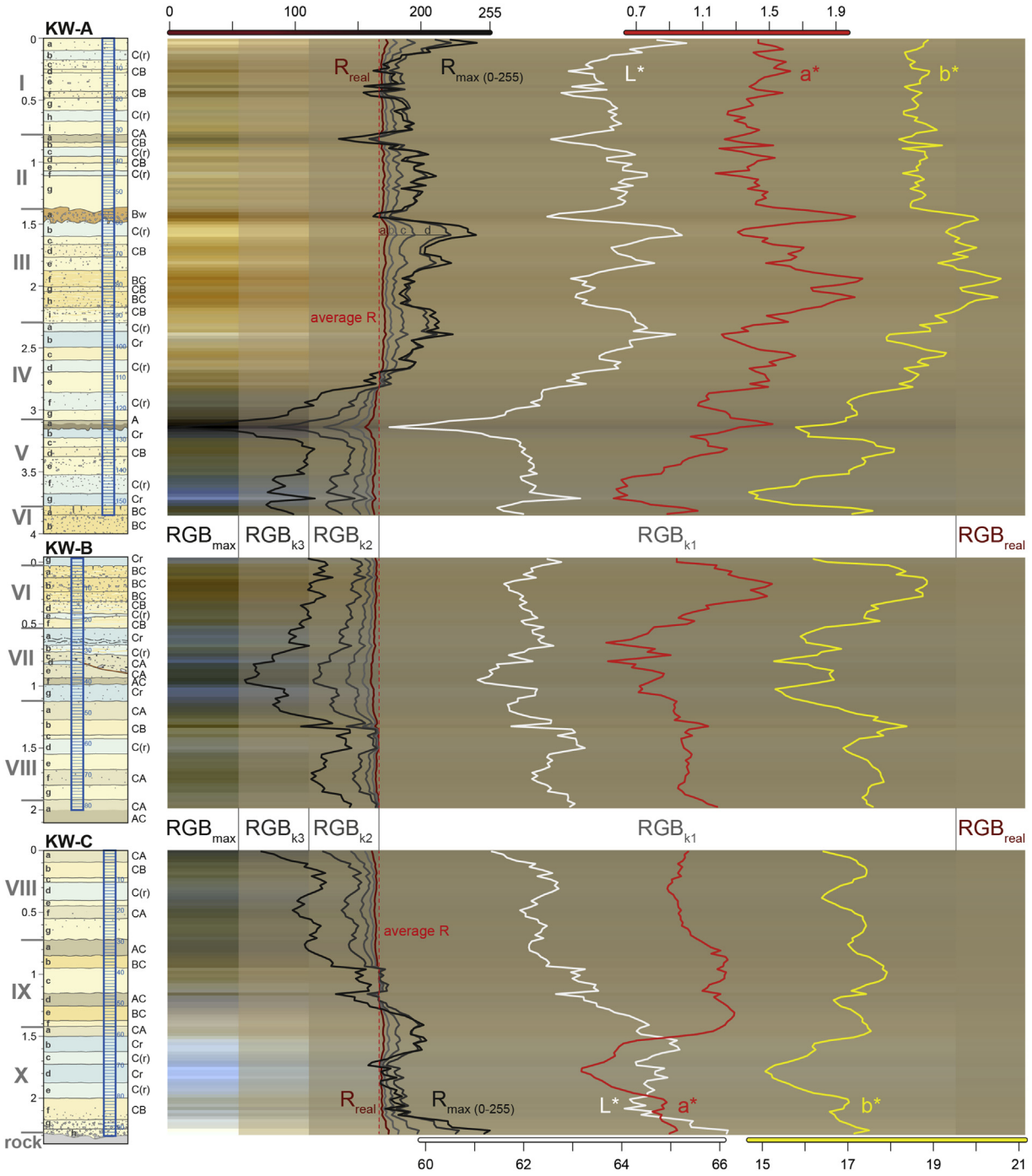

Fig. 5. Stratigraphy of the studied sections KW-A, -B, –C with pedological horizons (FAO, 2006; Sprafke, 2016), except for C horizons (loess sediments) and color data. Background shows from right to left the real RGB colors and four tuning steps ($RGB_{k1\ \ldots\ 3,\ max}$) of each sample. Left diagram exemplifies the variations of R_{real} and the four tuning steps ($R_{k1\ \ldots\ 3,\ max}$), as equally calculated for the parameters B and G. Color variables of the CIELAB color space indicate the lightness (L*), red (a*), and yellow (*b) components of individual samples (details lined out in section 3.3). (For interpretation of the references to color in this figure legend, the reader is referred to the Web version of this article.)

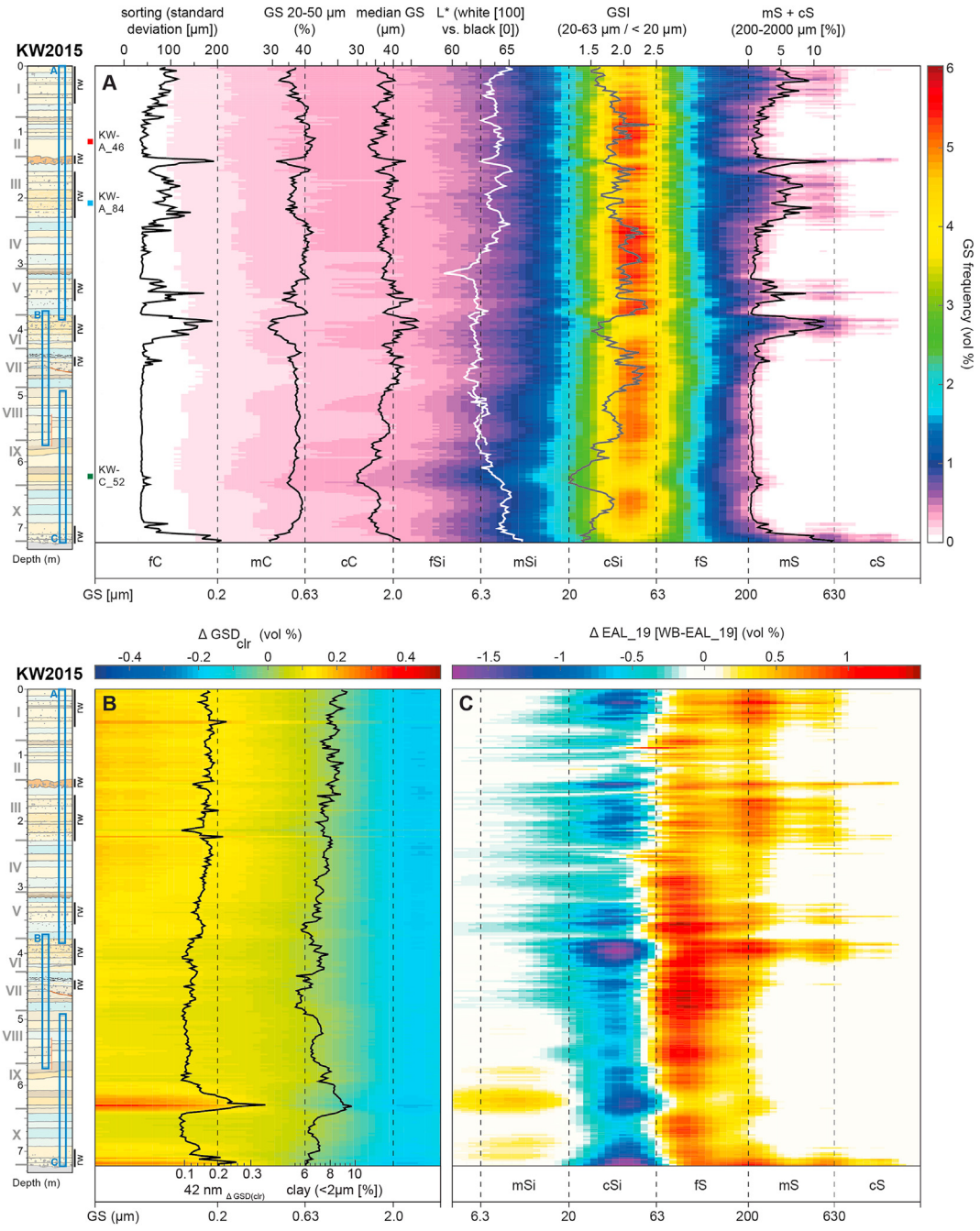

Fig. 6. KW2015 composite stratigraphy with the three samples shown in Fig. 7 and GS data. Note that the lower 12.5 cm of KW-A, the lower 52.5 cm of KW-B and the upper 30 cm of KW-C are excluded for these composites (full figure A: supplement Fig. S1). A: Heatmap visualizing the whole spectrum of GS data, the vertical curves represent the criteria for EAL_19 (preferably unweathered loess, for details see text), as well as GSI variations and medium to coarse sand contents. B: Heatmap (values < 4 µm) showing the ΔGSD_{clr} calculated to highlight the post-depositional enrichment of secondary clay minerals (Schulte and Lehmkuhl, 2018), vertical curves showing the ΔGSD_{clr} of the finest GS class (~42 nm) and clay values (<2 µm). C: Heatmap (values > 4 µm) showing the deviations of all individual samples of KW2015 to EAL19 (complete figures B + C: supplement Fig. S2).

powerful tool to reconstruct aeolian sedimentation dynamics (Antoine et al., 2009; Vandenberghe, 2013; Újvári et al., 2016; Schulte et al., 2018). Post-sedimentary in-situ alteration has to be taken into account, as well as reworking along slopes including the admixture of local material, e.g. by slope wash or solifluction (Sprafke et al., 2013; Schulte et al., 2016; Vandenberghe et al., 2018).

A Laser Diffraction Particle Size Analyzer (Beckman Coulter LS 13320, RWTH Aachen) measured the samples, applying the (Lorenz-)Mie theory (Fluid RI: 1.33; Sample RI: 1.55; Imaginary RI: 0.1) for calculating GS distributions (ISO 13320, 2009; Özer et al., 2010; Schulte et al., 2016). Organic matter was removed before measurement by treating the samples with 0.7 ml 30% H_2O_2 at 70 °C for several hours. This process was repeated for up to 3 days until a bleaching of the sediment occurred (Allen and Thornley, 2004). To keep particles dispersed, the samples were treated with 1.25 ml $Na_4P_2O_7$ (0.1 mol*l^{-1}) for 12 h on an overhead shaker (Pye and Blott, 2004; ISO 11277, 2009). This established routine allows comparison to GS data of over 20 Eurasian LPS, measured with the same protocol and device (cf. Fig. 7).

Heatmaps (Fig. 6A) visualize high-resolution GS data without

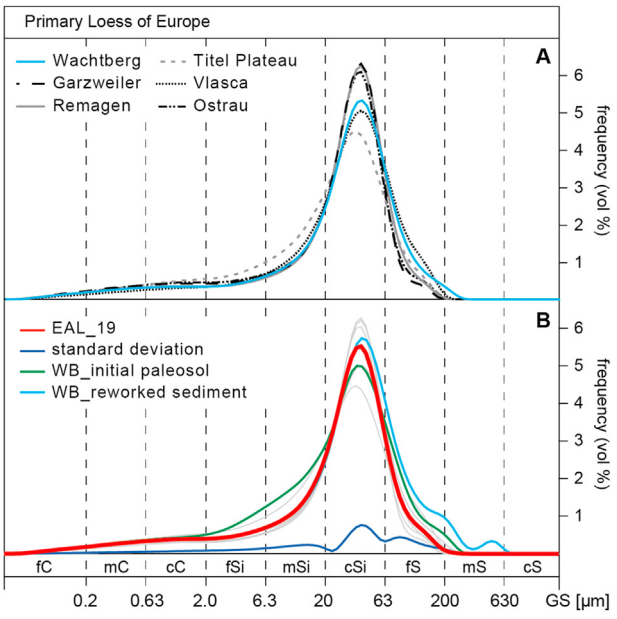

Fig. 7. GS distribution of European loess compared to KW2015 samples. A: Grain size curves from representative Central to SE-European loess (from KW2015 and the LPS Garzweiler, Remagen, Ostrau, Titel, Vlașca; locations in Fig. 1), B: EAL_19 (European average loess) is the average (including standard deviation) of the data shown in Fig. 7A compared to KW2015 samples affected by pedogenesis (KW–C_52) and reworking (KW-A_84) of KW2015 (stratigraphic positions in Fig. 6A).

the loss of vertical (samples with depth) or horizontal (116 GS classes) information (Schulte and Lehmkuhl, 2018). In addition to the GS data provided by the LS 13320 (GS classes according to ISO 14688, 2017), we calculated the grain-size index (GSI = [% 20–63 µm]/[% <20 µm]), which is interpreted as index for wind intensity (Rousseau et al., 2002; Antoine et al., 2009).

To visualize granulometric deviations from baseline loess due to variations in aeolian dynamics, pedogenesis and reworking, we define a standard loess from representative Central to SE-European sites stored in the RWTH GS database defined by the following criteria: 20–50 µm GS range, low scatter (sorting), light color (Fig. 6A), little MS enhancement (Fig. 8). This European average loess 2019 (EAL_19) is the average value of these preferably unweathered loess samples. KW-A 46 as closest analogue was added to the EAL_19 calculation. Deviations of each KW2015 sample from EAL_19 are visualized in a heatmap (>4 µm in Fig. 6C, complete spectrum in supplement Fig. S2).

Particles <1 µm are extremely underrepresented during aeolian accumulation and mainly form in situ. The complex refractive index considered by Mie theory takes into account more complex pattern of laser scattering, which are enhanced by pedogenically formed submicron minerals. The input values for the calculation vary for different mineral properties. For the Fraunhofer approximation (FH), however, the mineral properties are not taken into account. The difference of GS frequencies calculated with FH and with Mie (ΔGSD) quantifies clay mineral neoformed by chemical weathering (Schulte and Lehmkuhl, 2018). The variability of low concentrated GS ranges (e.g. the submicron) within percentage-frequency distributions can be misleading due to the compositional data effect (closed number space, constant sum of 100%) (Aitchison, 1986; Roberson and Weltje, 2014). Therefore, the vertical variability of bulk sample ΔGSDs is analyzed as centered log-ratio transformed GS differences. The centered log-ratio transformation (clr) is suitable to transform grain size distributions from closed to real number space (Roberson and Weltje, 2014). The clr-transformation is applied to both GSDs prior to the calculation of the differential. The resulting ΔGSD_{clr} is more robust against other GS influencing processes especially during sediment accumulation by sheet wash, saltation or enhanced background sedimentation (Schulte and Lehmkuhl, 2018).

3.3. Color measurements

Posterior to their sedimentation, dust particles are affected by in-situ alteration. Light-yellowish loess likely results from loessification during cold-dry climatic conditions (Pécsi and Richter, 1996; Sprafke and Obreht, 2016). Color changes along LPS primarily relate to pigmenting pedological processes that reflect paleoenvironmental conditions (Fig. 4), e.g. the reduction or oxidation of iron (grey/blue and yellow to red, respectively) or humification (black/brown) (Stevenson, 1982; Cornell and Schwertmann, 2003; Blume et al., 2010). Colored layers can also result from reworking of pigmented material. Spectrophotometers quantify color parameters more sensitive and objective than the human eye using defined color tables. The CIELAB color space variables L* (luminance, i.e. lightness [0–100]), a* (>0: red, < 0: green), and b* (>0: yellow, < 0: blue) and derived parameters like the Redness Index (Barron and Torrent, 1986; Viscarra Rossel et al., 2006) are increasingly used in loess research (Ding et al., 2002; Babek et al., 2011; Sprafke et al., 2013; Buggle et al., 2014; Gocke et al., 2014; Lukić et al., 2014; Vlaminck et al., 2016).

A Konica Minolta CM-5 spectrophotometer (RWTH Aachen) measured the air dried fine earth samples in a glass beaker on a circular field of 3.5 cm diameter. The procedure is identical to the one described by Gocke et al. (2014). L*, a*, and b* are the distinct color components plotted against RGB background colors (Sprafke, 2016). To facilitate the interpretation of the profile, a tuning of each RGB variable around its average value, proportional to the distance of the maximum and minimum values relative to the profile average, was done in three steps (RGB_{k1}, RGB_{k2}, RGB_{k3}). Maximum tuning (RGB_{max}) is achieved by transforming the RGB variables around their average values to the complete scale of this color space (0–255; Fig. 5).

3.4. Color-based stratigraphy

Variations of color parameters or their ratios reflect complex forming processes in the interplay of dust sedimentation, pedogenesis and reworking and their interpretation is not always straightforward. Sprafke (2016) uses color data to enhance field descriptions objectively, with stratigraphic units classified with master horizons (A, B, C and combinations) and their subordinate characteristics (FAO, 2006). Pedological subdivisions of LPS (Bronger, 1976, 2008; Schirmer, 2000, 2016) are reasonable, as visible changes in the stratigraphy of loess profiles are mainly related to post-depositional alteration of the deposits. Numerical color values support the precise separation of stratigraphic units and the classification of the units in relation to each other based on changes in certain color components (Sprafke, 2016). Color-based stratigraphy supports thorough field documentation but remains entirely descriptive and does not discriminate between in situ and reworked material.

C horizons represent the unaltered parent material (loess). A horizons are surface soil horizons characterized by increase in organic matter and thus often darker in color (lower L*-value) than loess. B horizons are subsurface soil horizons that show enhanced weathering and more brownish to reddish coloring (higher a*- and b*-values). The combination of two master horizon symbols indicates a transitional horizon, whereby the first letter characterizes

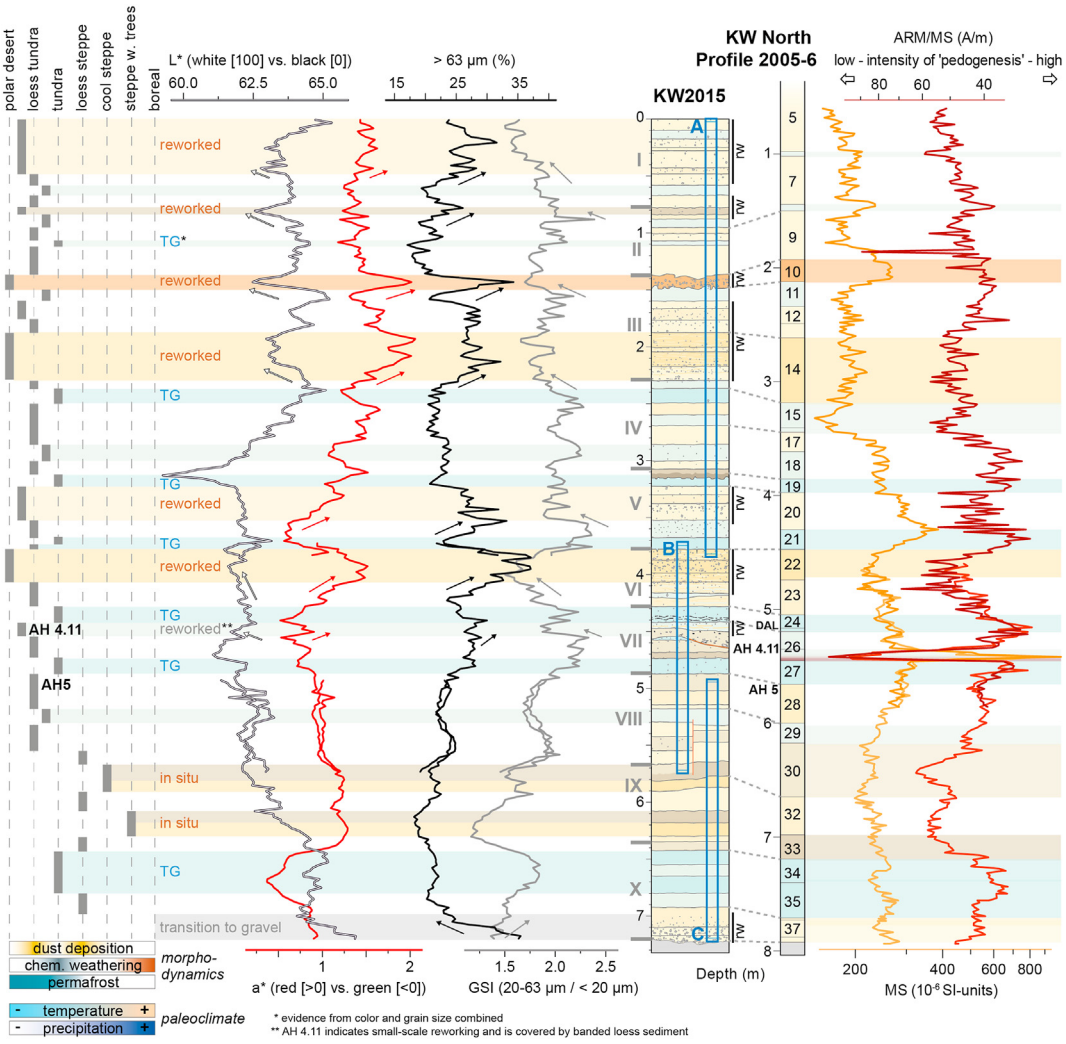

Fig. 8. KW2015 composite with representative color (L*, a*) and grain size variables (>63 µm, GSI) from the three studied profiles KW-A, -B, –C and KW2005 stratigraphy with MS variations (Hambach, 2010) shown for comparison. Note that reworked (rw) units are characterized by decreases in GSI and increases in sand contents (black and grey arrows), which allows the differentiation of in situ soils (unit IX) from soil-bearing brownish/darker sediment (color trends indicated by red and white arrows). Next to two oxidized terrestrial soils, there are seven tundra gleys (TG) related to in situ reduction. The left column of this figure provides the semi-quantitative paleoenvironmental interpretation (adapted from Heiri et al., 2014) based on reconstructed processes. Colors in the bars at the bottom indicate contribution of dust deposition (yellow), chemical weathering (grey for predominant reduction, brown for predominant oxidation, among other weathering processes), and permafrost (blue). These processes and environments lead to semi-quantitative paleoclimatic inferences, indicated below. (For interpretation of the references to color in this figure legend, the reader is referred to the Web version of this article.)

the dominant part (FAO, 2006), e.g. a BC is more brownish then a CB horizon. Units characterized by pale greyish colors (lower a*- and b*-, partly higher L*-values) are interpreted as Cr horizons of former Reductaquic Cryosols (IUSS Working Group WRB, 2014) forming in reductive environment above the permafrost table (Antoine et al., 2009). At present, temperate zone loess profiles do not contain cryic (perennially frozen) horizons and the reductaquic principal qualifier is not adequate for KW2015, as all Cr horizons are less than 25 cm thick (IUSS Working Group WRB, 2014). In the following, we refer to these specific loess paleosols as tundra gleys (Bibus, 1974; Frechen et al., 1999; Nigst et al., 2014; Moine et al., 2017).

In addition to the colored stratigraphic log, a transparent sand/gravel signature layer is added to the profile sketches, in order to illustrate units different from aeolian dust overprinted by pedogenesis of variable degree; these are units affected by higher wind strength or local reworking (Antoine et al., 2009; Vandenberghe et al., 2018).

4. Results

4.1. Field description

KW2015 exhibits no well-developed paleosol. Silty yellowish loess horizons with variable sand contents, partly accompanied by more brownish colors are repeatedly intercalated by pale horizons. The succession below the cultural horizon AH 4 is more homogenous with diffuse horizon boundaries, whereas the units above are more distinct and more variable. Most a priori defined GH (Händel et al., 2014; Terhorst et al., 2014) can be well identified (Fig. 8).

The KW2015 composite is subdivided into ten major units, labelled I–X, with subunits a, b, c etc. (Fig. 4 + 5). Unit X at the bottom, overlying the basal rock, is loess sediment comprising a thick pale horizon. Two weak brownish horizons divided by loess are present in the superimposed unit IX. Unit VIII consists of weakly differentiated loess sediments with incipient signs of reduction and humification. The reworked cultural layer AH 4.11 and superimposed sandier loess are located in between pale horizons (Unit

VII). Sandy, brownish loess sediments with wavy layers form unit VI, which is sharply cut by unit V, characterized by two pronounced bleached horizons with sandier loess in between. Centimeter-sized ice wedges at the boundary of units VI and V have revealed a polygonal network during the excavation. Loess sediments with more pale horizons are superimposed (Unit IV). The lower half of Unit III is characterized by brownish loess sediment with higher sand contents, microcracks and laminae. Unit IIIa is even stronger pigmented, has more coarse components and a wavy to pocket-like lower boundary. The loess sediments above are more homogenous, showing only weak differentiation, with pale horizons and a grey, sandier horizon in the upper part of unit II. Above we note an increase in coarse mineral components (unit I).

4.2. Color variations

The main trends of color variations (Fig. 5) summarize as follows: the lightness (L*) of the overall pale yellowish substrate is highest in the lowermost meter of the LPS, directly above the bedrock, and within the upper 2.7 m. Distinct maxima indicate bleached loess sediments (IIIb, IVb, Vg, VIIId), whereas minima are related to darker (IIa, Va, VIIe-f, IXa + d) or brownish horizons (IIIa, IIIf-h, VIb). Bleached horizons below 2.7 m often have relatively higher L*, but their main characteristic is reduced redness (a*) and yellowness (b*).

The a* and b* values oscillate in a similar way throughout most parts of the profile. In the upper 2.7 m there are higher a* and b* values compared to the loess sediments below. Maxima in these parameters well reflect the brownish sand enriched layers (IIIa, IIIf-h, VIb) and two incipient paleosols in unit IX. Minima are related to bleached horizons. Below AH 4 there are more variations in b* then a*. Unit Va records more expressed a*, relative to b*.

The visualized RGB colors confirm the presence of yellowish loess sediment with subtle color variations for KW2015, but tuned RGB values strongly enhance the contrast and detail (Fig. 5). Accordingly, the LPS is divided in three main parts, with the upper 2.7 m being more yellowish, reddish and lighter, the middle part more blueish and darker, and the lowermost 1.3 m again lighter. The distinct colors support the stratigraphic log (see section 4.4).

4.3. Granulometry

The heatmap of GS distribution (Fig. 6A for the KW2015 composite, complete figure in supplement Fig. S1) indicates an overall rather uniform character of the loess sediments with a general maximum in the coarse silt fraction around 40 μm. Lower concentrations in coarse silt are found in units with high contents of medium to coarse sand (units I, III, V, VI, base of X) or higher clay content (unit IX). The GS distribution of typical loess from KW2015 (sample KW-A_46) overall agrees with results from representative Central to SE-European loess (from the LPS Garzweiler, Remagen, Ostrau, Titel, Vlașca) measured until 2019 with the same device (Fig. 7A). Fig. 7B compares the GS distribution of this European average loess 2019 (EAL_19) to samples affected by pedogenesis (sample KW-C_52) and reworking (sample KW-A_84) of KW2015. Sample KW-C_52 from a weak paleosol (unit IXe, Fig. 4) has a higher clay content, a medium silt shoulder, and a main mode shift to smaller GS. Sample KW-A_84 from reworked deposits (unit IIIh, Fig. 4) has distinct medium to coarse sand modes.

Deviations of all individual samples from KW2015 to EAL_19 are visualized in a heatmap (Fig. 6C, for GS > 4 μm; complete figure in supplement Fig. S2). Next to marked increases in medium to coarse sand or clay in distinct units, we note that the sequence below 2.7 m (units IVe to X) has slightly higher fine sand contents compared to the EAL_19. The sequence above 5 m (units I to VII), has a higher variability in GS distribution and overall slightly lower amounts of medium silt. This increase in GS variability is also shown in different GS parameters, with examples in Fig. 6A. Contrary to the GSI variation in the LPS Nussloch (Antoine et al., 2009), the GSI variations of KW2015 do not always correlate to the sand contents (Fig. 8), which is especially visible in units with higher amounts of medium to coarse sand and peaks in GS median (Fig. 6A).

Clay contents range between 6 and 10% with maxima in unit IX and minima in unit VII. Noteworthy is a constant increase in clay from unit VII (6%) to the top of the sequence (9%). The ΔGSD_{clr} values as measure for the amount of pedogenic clay (Schulte and Lehmkuhl, 2018) are shown as heatmap and represented by the 42 $nm_{\Delta GSD(clr)}$ curve in Fig. 6B (for GS < 4 μm; complete figure in supplement Fig. S2) Values range around zero in the entire dataset. Between unit I and unit V the ΔGSD_{clr} signals for the submicron GS range are slightly increased. Maxima are at the very bottom of the profile, especially in unit IXd-f, the weak paleosol (AC/BC) in the lower part of unit IX. Interestingly, the subunits characterized by reworked brownish material (e.g. IIIa, VI) show lower values of the ΔGSD_{clr} compared to surrounding layers (Fig. 6B).

4.4. Stratigraphy of the KW2015 composite

The stratigraphy of KW2015 is based on detailed field logging supported by high-resolution colorimetric data and complemented by a high-resolution GS data set. 10 major units (I-X) were visible in the field, while color data facilitate the distinction and classification of up to 9 subunits per major unit (a-i; ig. 4). Most horizons of KW2015 classify as C horizons or as transitional to A (CA/AC) or B (CB/BC) horizons, depending on the contribution of dark or brown colors, respectively. Pale horizons with low L* and/or low a*/b* values classify as C(r) or Cr horizon depending on their intensity. Only two horizons of the whole section are sufficiently distinct from loess to classify without a C master horizon symbol: Unit IIIa is a brownish sandy horizon labelled GH 10 in the field assessment, classified as Bw horizon. Unit Va, the very dark horizon on top of GH 19, was interpreted as fossil manganese band by Terhorst et al. (2014), but this was not confirmed by their geochemical data. Until composition and genesis of unit Va are clarified it is classified as A horizon based on its color.

5. Discussion

5.1. Color-based loess stratigraphy and granulometry

Pale yellow, aggregated, carbonate bearing substrate dominated by coarse silt that formed mainly by accumulation of windblown dust constitutes the original baseline material in LPS (Pécsi, 1990; Pye, 1995; Sprafke and Obreht, 2016). Loess GS variations primarily reflect changes in sedimentation dynamics, whereas color reflects mainly post-depositional alteration (pedogenesis). Both parameters for unravelling this dynamic interplay are now available in high resolution from the LPS Krems-Wachtberg and support a robust stratigraphy (KW2015). Understanding the complex pedosedimentary evolution is prerequisite to paleoenvironmental reconstructions.

Quantified color variations support a detailed and robust stratigraphic log for weakly differentiated loess profiles (Sprafke, 2016). Master horizons (A, B, C and combinations) and subordinate characteristics (h, r, t, w etc.) from pedology (FAO, 2006) capture the high stratigraphic variability of KW2015 (Fig. 4 + 5). This approach is chosen for a robust subdivision of complete loess profiles, whereas reconstructions of (sub)unit evolution requires

morphological observations and further data (e.g. from granulometry). Color data strongly support the definition of boundaries and a consistent classification of units, but do not replace profile or drill core documentation. . KW2015 not only reproduces, but considerably refines the GH stratigraphy defined during the archeological excavations (Händel et al., 2014) and provides a consistent scientific terminology (Fig. 8).

Six well-developed pale horizons interpreted as tundra gleys in units IV-VII and X, three reworked brownish yellow layers in units III and VI and two weak paleosols in unit IX were clearly visible in the field, whereas less developed units could be robustly defined based on color data (Fig. 4). It is important to note that the horizon designations from pedology used here are descriptive and not genetic. Interpreting the LPS evolution requires a differentiation of paleosols from reworked soil material based on field observation and GS data. The dark and brownish AB and BC horizons below AH 4 show increases in finer GS indicating pedogenesis, whereas all BC and Bw horizons above AH 4 contain higher proportions of sand and gravel, admixed during soil reworking (Fig. 8).

The detailed KW2015 color-based stratigraphy complemented by granulometry differentiates LPS units according to the predominance of aeolian, pedogenic or slope processes during their formation, which helps to select adequate proxies representing these process groups. Such differentiation is relevant for LPS locations with an overall higher weathering degree, lower sedimentation rates and/or variable topography. Soil formation is a downward oriented alteration of already deposited sedimentary layers (Rousseau et al., 2017b) and slope processes lead to erosion and reworking of sediment and soil (Sprafke et al., 2014). Sedimentological approaches, i.e. using vertical LPS parameter variations as quantitative estimates for process intensities and factors through time (commonly referred to as proxies) are applicable, when the predominance of aeolian sedimentation is verified (C, CA and CB horizons, if not reworked). In all other cases, pedogenesis has to be included in parameter interpretation. The stratigraphy of KW2015 indicates numerous phases of pedogenesis and reworking, therefore a differentiated approach to unravel its formation is required.

5.2. LPS proxies and Krems-Wachtberg reality

5.2.1. Granulometry

Throughout KW2015, coarse silt, typical for loess (Pye, 1995; Pécsi and Richter, 1996), is the predominant GS (Fig. 6A). Compared to the EAL_19 measured with the same device only the samples between 0.5 and 1.4 m and between 2.3 and 3.2 m of KW2015 have a comparable frequency in the mode fractions (light colors in the coarse silt fractions of Fig. 6C). Unit II has the closest match to typical loess from Central Europe and may be defined as local reference loess. Slightly larger and more frequent modal fractions likely indicate higher local wind-speed or closer deflation centers (Nugteren and Vandenberghe, 2004; Újvári et al., 2016). Additional submodes in the medium to coarse sand range (units I, III, V, VI, and the bottom of the LPS) result from admixtures of local coarse material by sheet wash or solifluction (Sprafke et al., 2013; Zeeden et al., 2016), which is indicated by layering of units III and VI and partly sharp unit boundaries.

Deviations in GS along LPS are usually related to changes in aeolian dynamics during the formation of the record (Vandenberghe, 2013; Újvári et al., 2016). GS ratios represent certain process groups more adequate than variations of GS classes, due to the compositional data effect. The GSI unravels variations in wind intensity (Antoine et al., 2009), if in-situ alteration resulting in clay mineral formation and local reworking are excluded (Schulte et al., 2018). At the LPS Nussloch, increases of the GSI are accompanied by higher fine sand contents due to a shift of the GS mode into the direction of coarser GS resulting from higher wind intensity (Antoine et al., 2009). At KW2015 only the lower part of the sequence (units VII-X) has comparable patterns in both, GSI and sand content. Above units with highest sand contents are accompanied by lower GSI (Fig. 8). Local reworking (units marked by "rw" in the KW2015 composite) along the slope mobilized coarse material, which creates distinct medium to coarse sand modes (Fig. 6A), independent of smaller shifts in the GS mode by changes in wind intensity.

Sheet wash mobilizes fine sand to coarse silt better than more cohesive finer fractions, which strongly affects the GSI, as coarse silt (20–63 μm) is the numerator of this ratio. This proxy of past aeolian dynamics is apparently inadequate for settings, where coarser components are admixed by non-aeolian processes. This finding highlights that GS proxies require a critical evaluation related to the regional climatic and local topographic context (Schulte et al., 2018). KW2015 sand contents are the most suitable parameter to reflect local changes between morphodynamic activity (open vegetation cover, intensified wind-speed and reworking) and stability (closed vegetation cover, low wind-speed and possibly pedogenesis; Fig. 9).

The overall clay contents show relative maxima in the weak paleosols of unit IX which can be attributed to pedogenesis, given the brownish pigmentation and a weak soil structure. The slight clay increase from unit VII to the top of the sequence likely reflects a change in dust source, as our stratigraphy does not point to significant pedogenesis in this part of the sequence, except reduction leading to tundra gley formation. Terhorst et al. (2014) report a marked increase in carbonate contents from unit VI (20–25%) to the top (35–40%), which may contribute to the clay fraction if finely dispersed during loessification (Sprafke and Obreht, 2016). Absolute clay contents as proxies for weathering intensity areonly recommendable after verification of sedimentary homogeneity and cross-checking with other parameters.

The ΔGSD_{clr} signature of the LPS is a direct indicator for post-depositional chemical weathering processes and successfully applied in several Central European LPS, e.g. Garzweiler, Düsseldorf-Grafenberg, Ringen or Frankenbach, all located in the Rhine catchment (Zens et al., 2018; Schulte and Lehmkuhl, 2018; Fischer et al., 2019). These LPS have ΔGSD_{clr} values around 2 to 7 (dimensionless) in well-developed interstadial soils, which is considerably more than for KW2015, where ΔGSD_{clr} values range around zero in the entire dataset (Fig. 6B, left side). The incipient paleosol (AC/BC) in the lower part of unit IX is the only paleosol with a pronounced signature of the ΔGSD_{clr}, indicating the formation of clay minerals by silicate weathering. The positive deviations to EAL_19 in the mSi (medium silt) fractions are probably due to pedogenic formation of stable microaggregates (Fig. 6C). These deviations occur in the entire Unit IX. The slightly increased values between Unit I and Unit V (visible in the 42 $nm_{\Delta GSD(clr)}$ curve) may result from slight chemical weathering or a change in the dust source. The latter is more likely, as sediments interpreted as loess or tundra gleys are often not altered by considerable silicate weathering when a carbonate buffer is abundant (Blume et al., 2010).

5.3. Colors and magnetic susceptibility

Throughout the sequence, color parameters are more variable than ΔGSD_{clr}, showing their high potential sensitivity for initial pedogenesis. Pigmenting soil forming processes like oxidation, reduction or humification (Cornell and Schwertmann, 2003; Blume et al., 2010) can already take place in the presence of carbonate that largely buffers further chemical weathering (cf. Bronger, 1976). However, colors cannot distinguish soil from soil sediment.

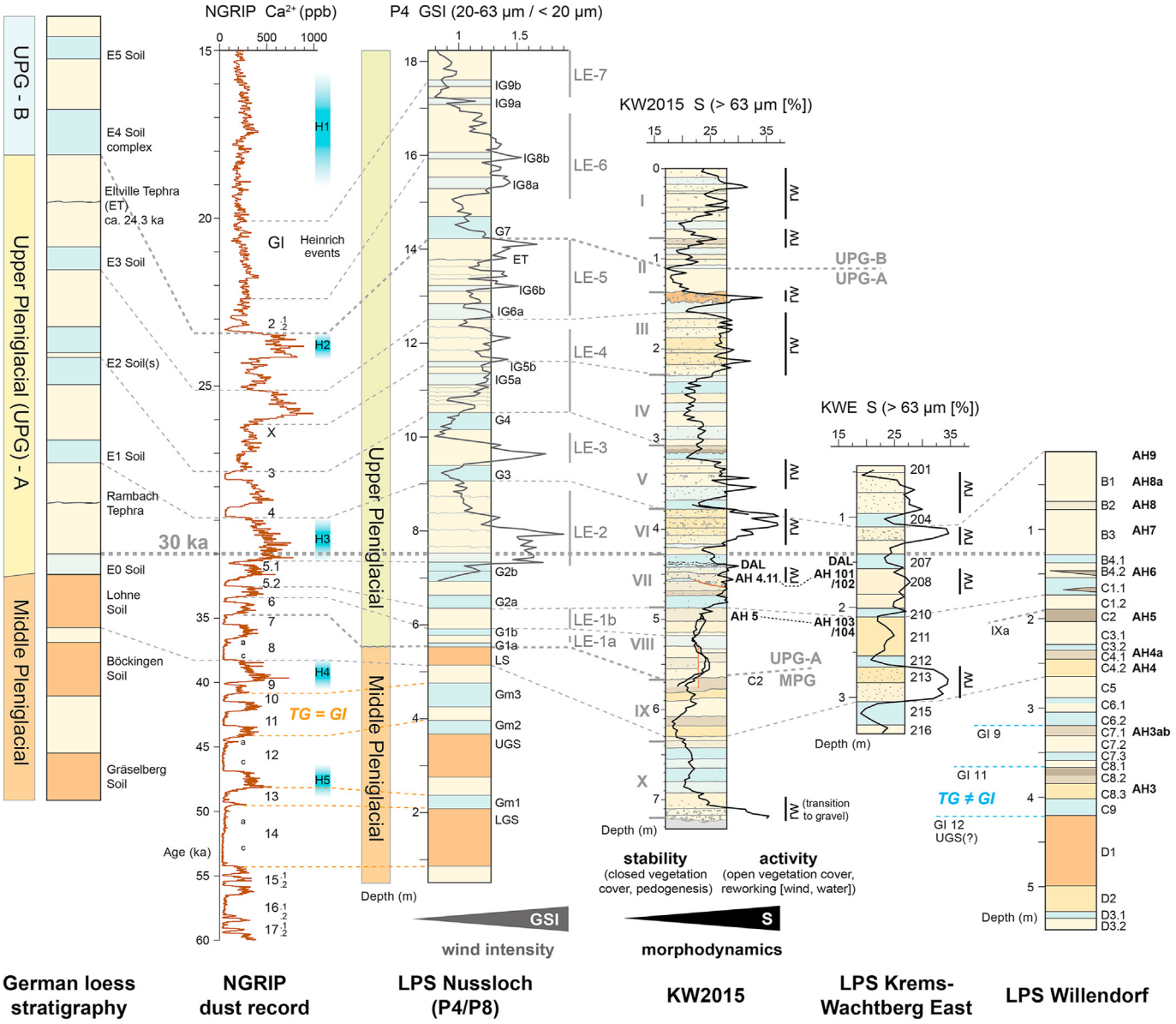

Fig. 9. Correlation of KW2015 with the nearby LPS Krems-Wachtberg East (Meyer-Heintze et al., 2018), the LPS Willendorf (Nigst et al., 2014, redrawn), the Nussloch reference LPS (Moine et al. (2017, redrawn) with GSI plot from P4 and loess events (LE) indicated (Antoine et al., 2009), NGRIP dust record (Rasmussen et al., 2014; note a change of the age scale at 30 ka), and the German loess stratigraphy (Lehmkuhl et al., 2016). Age of Eltville Tephra from Zens et al. (2018). Sand contents of KW2015 and Krems-Wachtberg East (Meyer-Heintze et al., 2018) reflect the geomorphic response of these profiles to paleoenvironmental changes. Note the disagreement in correlation of MPG tundra gleys to GI, i.e. the Nussloch model (TG = GI; Moine et al., 2014) and Willendorf model (TG ≠ GI; Nigst et al., 2014) discussed in the text.

Interestingly, the ΔGSD_{clr} values are low in reworked units of KW2015, suggesting that aquatic reworking removes clay from soil sediments, whereas enough iron oxides remain as brownish pigments, attached to the remaining silt and sand grains.

Color variations are increasingly applied in loess research as proxy for paleoenvironmental evolution (Lukić et al., 2014; Krauss et al., 2016; Vlaminck et al., 2016). The Redness Index (RI) or a* are used to detect horizons affected by pedogenesis resulting in the formation of iron oxides as reddish or brownish pigments (Lukić et al., 2014; Vlaminck et al., 2016). Calculations of the RI recognize that increasing hematite contents not only increase a* but also reduce the lightness of a soil and thus include L* in the denominator in the formula for the RI (Viscarra Rossel et al., 2006). Being sensitive to dark pigments, the RI is not applicable to LPS with humic horizons (Sprafke, 2016). For KW2015, we note that the maxima in reddening are related to reworked layers in unit III. Dark red components, partly as coatings around sand grains indicate iron remobilization in this better drained material, but they may also originate from weathered Neogene gravels exposed upslope on the Wachtberg hill (Fuchs and Grill, 1984). Unit VI is equally reworked, with a maximum peak in a*, relative to the surrounding material. Only in unit IX the increases in a* seem to result from in-situ oxidation (Fig. 8).

The overall increase in L* in the upper 3 m (units I-IV) can be explained with a 10–15% increase in carbonate contents (white pigment) as measured by Terhorst et al. (2014). All tundra gleys above AH 4 have distinct local peaks in carbonate (c. 3–8% more compared to surrounding layers), which agrees with observations of Meyer-Heintze et al. (2018) from a sequence close-by and can be explained by capillary enrichment of $CaCO_3$ during reduced

conditions (Cilek, 2001). The tundra gley below AH 4 does not show an increase in carbonate and the dataset of Terhorst et al. (2014) does not reach pale horizons below. In the Krems region both exist, thin pale carbonate rich tundra gleys and thicker blueish ones without increase in carbonate (Sprafke, 2016). Overall, there is no clear connection between tundra gley formation and carbonate dynamics in Central Europe (Antoine et al., 2009; Krauss et al., 2016), but possibly high loess carbonate contents result in calcite enriched tundra gleys, whereas tundra gleys in loess with low carbonate contents have reduced calcite contents.

The characteristic feature of tundra gleys are lower a* and b* values due to iron reduction, but changes in L* seem to depend mainly on the presence of carbonate. We do note, however, a steady increase in L* in the lower 2 m of the sequence, which likely relates to slight reduction processes due to higher pore water contents close to the bedrock, resulting in a slight overprinting of the color record.

All these qualitative observations suggest that color variations need to be carefully interpreted, before they can be used as paleoenvironmental proxies. Relative variations of color and further parameters (e.g. field observations, GS distributions) have to be considered for stratigraphy and a process-based interpretation of the pedosedimentary evolution of KW2015 (section 5.3). RGB tunings coupled with L*, a*, and b* variations are useful to delimit and classify stratigraphic units. Caution is required to not over-interpret strongly tuned color plots, therefore comparison to field observations is required (Sprafke, 2016). RGB tuning around the profile average works well for KW2015 (Fig. 5), but sequences with well-developed paleosols require the tuning around a standard loess color. To date there are no unified routines for loess colorimetry to provide robust color tuning as a tool to facilitate loess stratigraphy, but our results indicate a high potential for this approach.

Environmental magnetic parameters from the LPS Krems-Wachtberg (Hambach, 2010; Groza et al., 2019) are sensitive to most stratigraphic units of KW2015 (Fig. 8). Tundra gleys of units I, VII and X are represented by considerably lower ARM/MS ratios indicating a higher intensity of pedogenesis (Hambach, 2010). However, the weak unit IX paleosols have no clear correspondence in the environmental magnetic record and several stratigraphic units have ambiguous responses to these data. Connecting the environmental magnetic parameters to the KW2015 stratigraphy may strongly enhance the potential of these proxies.

5.4. LPS evolution and paleoenvironmental inferences

KW2015 sand contents inform about local variations between morphodynamic activity and stability, but not in detail about the complex interplay of aeolian sedimentation, pedogenesis, and reworking in the context of the local paleoenvironmental evolution. Complex terrestrial records require a reconstruction of the forming processes based on the integration of complementary parameters (Meszner et al., 2013; Sprafke, 2016; Meyer-Heintze et al., 2018). Unit-based reconstructions benefit from additional paleoenvironmental proxies (Kukla, 1977; Haesaerts et al., 1996, 2007), whereas our interpretation is entirely based on reconstructing the pedosedimentary evolution.

Fig. 8 (left side) summarizes the semi-quantitative paleoenvironmental conditions during the formation of KW2015 reconstructed from forming processes of stratigraphic units. The scheme developed for the LPS Willendorf by Heiri et al. (2014) was slightly adapted to better include representative paleoenvironments. It differentiates dust deposition taking place in cold steppe (without permafrost) or in tundra (with permafrost), a classification that depends on the local stratigraphic context, i.e. the paleosols developed therein and further paleoenvironmental information. At KW2015 we note a marked change from terrestrial soils and smooth GS variations (unit IX) to the predominance of tundra gleys and more variable GS pattern (units I-VIII), which we interpret as major climatic transition that goes along with the onset of permafrost and more active floodplains as local deflation centers (Moine et al., 2017). Tundra gleys in this part likely represent milder conditions, with reduced dust deposition (Antoine et al., 2009). The tundra gley of unit X likewise indicates a phase of permafrost presence.

On the cold end of the paleoenvironmental scale (Fig. 8) we introduce a new category without dust accumulation or pedogenesis under the presence of permafrost, which corresponds to a polar desert (cf. Sirocko et al., 2016). This is an open landscape with almost no vegetation cover, with no relevant dust deposition, but episodes of reworking by slope wash. In the geological setting of Krems-Wachtberg these processes result in the admixture of coarse material of upslope weathered gneiss and Neogene gravels.

KW2015 rests on crystalline rock that is partly covered by fluvial gravels, which are reworked and mixed with initial aeolian dust. The thick tundra gley of unit X formed from loess under reducing conditions due to the presence of permafrost impeding drainage (Antoine et al., 2009; Terhorst et al., 2015). Unit IX represents two weak paleosols with brownish pigmentation, interrupted by dust deposition. The lower paleosol shows an advanced development involving clay mineral neoformation as indicated by an enhanced ΔGSD_{clr} value and positive deviations of EAL_19 in the mSi (medium silt) fractions. The latter is likely due to the pedogenic formation of stable micro-aggregates. Unit VIII represents a strong increase in dust deposition, interrupted by weak pedogenesis, with unit VIIId as weak tundra gley. The slightly darker pigmented unit VIIIf has a higher sand content and is therefore interpreted as short scale (maybe aeolian) reworked incipient topsoil, rather than an in-situ humification.

Unit VII encompasses cultural layer AH 4, surrounded by two well-developed tundra gleys that indicate the presence of permafrost and negligible dust deposition. For AH 4 itself, we assume the presence of permafrost and dust deposition as dominating process (Händel, 2017). Note that KW2015 does not assess the in situ occupation layer AH 4.4/4.3 as this unit did not extend so far. Topographically, the sampling locations are positioned downslope of the occupation layer, and the assessed part of AH 4 (AH 4.11) contains archeological material redeposited shortly after the site was abandoned, indicated by the scatter of radiocarbon ages related to AH 5 and AH 4.4/4.3 (Fig. 3; Händel, 2017).

Unit VI consists of reworked material and can be attributed to a dry open landscape with sparse vegetation cover facilitating surface processes. Unit V encompasses two further tundra gleys, interrupted by dust deposition and a phase of reworking indicated by coarse material admixture. Unit IV formed by increased dust deposition with at least one minor interruption in the lower part (unit IVf) and a major interruption marked by a tundra gley at the top (IVa-b). The two well-visible brownish horizons in unit III with higher shares of coarse material result from intensified slope processes in a dry open landscape and were interrupted by a phase of dust deposition before a short period of stability (unit IIIb). Later dust deposition (unit II) was interrupted by incipient tundra gleys and an episode of reworking (IIa). Unit I consists of loess, partly with signs of reworking in an open landscape (Fig. 8).

5.5. Chronological framework and correlations

Detailed stratigraphic logs of LPS are prerequisite to understanding profile evolution in the context of local

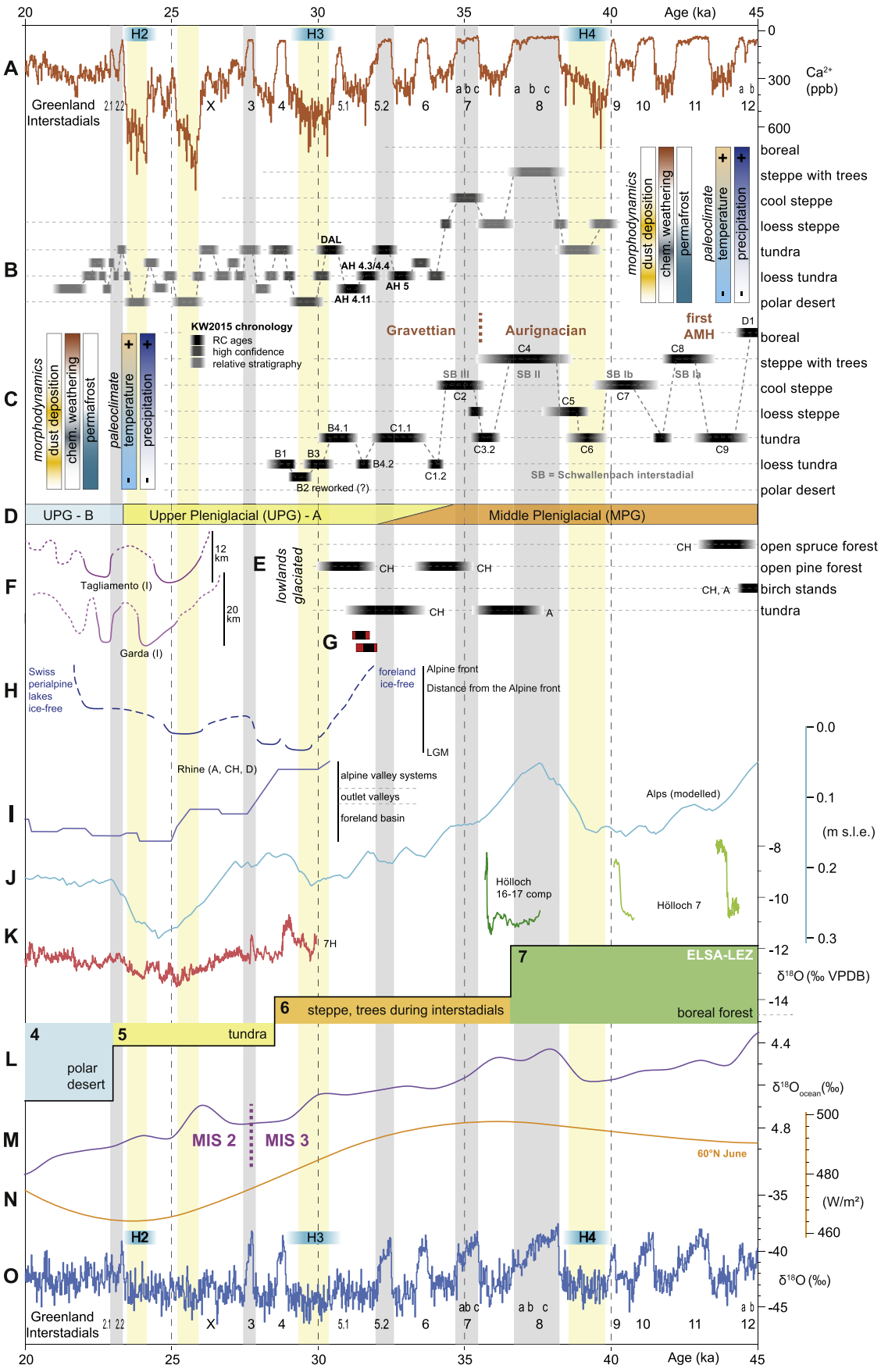
Age (ka)
A
Greenland Interstadials
H2
H3
H4
Ca2+ (ppb)
B
DAL
AH 4.3/4.4
AH 5
AH 4.11
morphodynamics
dust deposition
chem. weathering
permafrost
paleoclimate
temperature
precipitation
boreal
steppe with trees
cool steppe
loess steppe
tundra
loess tundra
polar desert
C
KW2015 chronology
RC ages
high confidence
relative stratigraphy
Gravettian
Aurignacian
first AMH
SB = Schwallenbach interstadial
D
UPG - B
Upper Pleniglacial (UPG) - A
Middle Pleniglacial (MPG)
F
Tagliamento (I)
Garda (I)
E
lowlands glaciated
CH
A
open spruce forest
open pine forest
birch stands
tundra
G
H
Swiss perialpine lakes ice-free
foreland ice-free
Alpine front
Distance from the Alpine front
LGM
I
Rhine (A, CH, D)
alpine valley systems
outlet valleys
foreland basin
Alps (modelled)
(m s.l.e.)
J
Hölloch 16-17 comp
Hölloch 7
K
7H
δ18O (‰ VPDB)
7
ELSA-LEZ
6
steppe, trees during interstadials
boreal forest
4
polar desert
5
tundra
L
δ18Ocean (‰)
M
MIS 2
MIS 3
60°N June
(W/m²)
N
O
δ18O (‰)

paleoenvironments (Haesaerts et al., 1996, 2007; Antoine et al., 2009, 2013; Terhorst et al., 2015). A chronological framework is required to differentiate process intensity from process duration and to allow for correlations to other paleoenvironmental records that lead to an improved understanding of paleoclimatic evolution and regional effects of climatic changes (Sprafke, 2016). The available geochronological dataset from Krems-Wachtberg was outlined in section 2.2 and is shown in Fig. 3.

The age model of Hambach et al. (2008) used by Terhorst et al. (2014) relies on variations of magnetic parameters and their correlation to the NGRIP oxygen isotope variations. Partly inconsistent behavior of magnetic parameters compared to our stratigraphy and a 1–3 ka younger age of AH 4 based on radiocarbon dating suggest a modified age model. Luminescence ages are the only absolute age control from the entire LPS Krems-Wachtberg (Lomax et al., 2014; Groza et al., 2019), but relatively large error bars and methodological inconsistencies do not allow for precise correlation with millennial scale paleoclimatic reference records, e.g. the NGRIP dust record (Fischer et al., 2007; Rasmussen et al., 2014). The 19 radiocarbon ages with smaller errors seem reliable, being well within the dating range of this method (Nigst et al., 2014).

The available radiocarbon ages from AH 4 and surrounding horizons can be used as references to tentatively evaluate the reliability of the luminescence ages as calibration insecurities are far smaller than OSL errors (Fig. 3). Overall, the ages of the three luminescence laboratories involved in the study of Lomax et al. (2014) agree within error, but quartz fine grain optically stimulated luminescence (OSL) ages appear as best match to the radiocarbon ages. Polymineral fine grain infrared stimulated luminescence (IRSL) ages appear systematically younger (although no fading was detected in the laboratories) and quartz coarse grain OSL ages seem slightly too old (cf. Lomax et al., 2014). Despite these insecurities, the data indicate a quasi-continuous sedimentation between c. 40–20 ka and suggest a stratigraphic comparability to well-dated LPS of the same period for the upper and lowermost parts of KW2015, with less robust age control.

Fig. 9 compiles stratigraphic information from the nearby LPS Krems-Wachtberg East (Meyer-Heintze et al., 2018), the LPS Willendorf c. 25 km upstream the Danube in the Wachau Valley (Haesaerts et al., 1996; Nigst et al., 2014), the LPS Nussloch close to Heidelberg as Central European reference LPS and the German standard loess stratigraphy (Lehmkuhl et al., 2016; Zens et al., 2018). The 30 ka line is used as a common reference for all profiles. This reveals overall similarities in the well-resolved stratigraphic successions and regional/local modifications. Especially when KW2015 is compared to the well-dated LPS Nussloch (Moine et al., 2017) we note some striking similarities and characteristic deviations. The incipient paleosols in unit IX of KW2015 correlate well with the Lohne soil at Nussloch. Both records contain a comparable number of tundra gleys, which agree in their relative stratigraphic position and intensity. Pronounced loess events (LE), marked by GSI peaks (Antoine et al., 2009), seem to correlate to reworked horizons of KW2015 marked by higher amounts of sand (section 5.2, Fig. 8). These features suggest to largely adapt the Nussloch chronostratigraphy for those parts of KW2015 with limited absolute age control, with modifications discussed in the following.

5.6. Local environment vs. catchment morphodynamics

KW2015 records millennial-scale paleoenvironmental responses to northern hemispheric climatic changes with specific successions of loess, paleosols and, reworked units. The low weathering degree of unit IX compared to upper MPG soils in the Rhine catchment indicated by the ΔGSD_{clr} (Zens et al., 2018) can be explained by the continental location of KW2015 at the eastern margin of the Bohemian Massif. Beyond in-situ alteration, the influence of local topography and catchment morphodynamics requires consideration (Smalley et al., 2009).

Reworked layers at KW2015 and Nussloch LE are local signals for the coldest conditions during the UPG, which correlate with NGRIP dust peaks (Moine et al., 2017) and are partly related to Heinrich events (Fig. 9) (Sanchez Goñi and Harrison, 2010; Rasmussen et al., 2014). During these coldest conditions, maritime moisture of Western Central Europe likely supported Western Alpine glacier activity and enhanced silt production, dynamic braided rivers in the Rhine catchment that transport and temporarily expose silt, and a vegetation cover to efficiently trap dust (Pye, 1995; Smalley et al., 2009). Additional dust at Nussloch originates from Western Europe and was brought in by frequent dust storms; a system coupled to large scale dust dynamics recorded in the NGRIP dust record (Antoine et al., 2009; Moine et al., 2017). Krems at the eastern margin of the Bohemian Massif receives overall less maritime moisture and is located within the Danube catchment, which mainly drains the more continental Eastern Alps. During the coldest periods of the UPG the scarcity of vegetation facilitated reworking and reduced the local potential to trap aeolian dust, which was likely less efficiently produced in the catchment and transported downstream before aeolian entrainment.

Nussloch UPG tundra gleys separate LE and represent milder conditions, correlating to and partly even outnumbering GI (Antoine et al., 2009; Moine et al., 2017). At Willendorf, a record with higher resolution during the MPG, tundra gleys are thought to represent the coldest conditions during the last glacial period (Haesaerts et al., 1996; Nigst et al., 2014). These contrary interpretations of tundra gleys are based on LPS with detailed stratigraphic records and good age control. For KW2015, chronological information from AH 4 and surrounding units, together with stratigraphic reasoning are in strong support for the age model of Nussloch for the UPG and Lohne soil equivalent (units I-IX), whereas the tundragley below (unit X) is problematic. OSL quartz fine grain ages, which are reliable in tundra gleys around AH 4, suggest a sedimentation age of 39.1 ± 3.1 ka for the basal tundra gley parent material, matching Heinrich event 4 (Lomax et al., 2014). A correlation with Nussloch Gm3 (GI 10–11) requires a generous interpretation of the OSL age error and implies an absence of Heinrich event 4 in KW2015. The key question is, does unit X represent a milder phase (e.g. GI 9 and 10) of an MPG dominated by permafrost, with few oxidized paleosols representing the longest GI (Rousseau et al., 2017a), or does it represent climatic

Fig. 10. Paleoenvironmental and -climatic context of KW2015. A: NGRIP dust record from Rasmussen et al. (2014) as indicator of large scale Northern Hemispheric dust dynamics. B: Semi-quantitative paleoenvironmental information (cf. Fig. 8) from the LPS Krems-Wachtberg. C: Same as B for the LPS Willendorf with Palaeolithic techno-complexes added (modified from Heiri et al., 2014; Nigst et al., 2014). D: Main stratigraphic units of Central European loess stratigraphy (Lehmkuhl et al., 2016). E: Alpine foreland pollen records from Austria (A) and Switzerland (CH) as compiled by Heiri et al. (2014). F: S Alpine piedmont lobes Garda and Tagliamento from Monegato et al. (2017). G: Radiocarbon ages (calibrated with IntCal20; Reimer et al., 2020) from the gravel pit Mils close to Baumkirchen from Spötl et al. (2013) marking the onset of the Alpine UPG. H + I: Rhine-Linth glacier fluctuations compiled by Heiri et al. (2014) and Preusser et al. (2011), respectively. J: Modelled Alpine ice volume in meters of sea level equivalent (m s.l.e.) by Seguinot et al. (2018). K: Alpine speleothem $\delta^{18}O$ variations from Siebenhengste Cave (7H; Luetscher et al., 2015) and Hölloch (Moseley et al., 2014). L: ELSA landscape evolution zones based on proxy evidence from Eifel Maar lakes (Sirocko et al., 2016). M: Global stack of marine oxygen isotope variations by Lisiecki and Raymo (2005) with MIS 3/2 transition marked based on Andersen et al. (2006). N: Summer insolation at 60°N from Berger and Loutre (1991). O: NGRIP oxygen isotope record as paleoclimatic reference for last glacial NW European suborbital paleoclimate fluctuations (Rasmussen et al., 2014).

deterioration (Heinrich 4) within an MPG otherwise largely free of permafrost?

It is reasonable to correlate paleosols of more advanced development to longer GIs (Rousseau et al., 2017a), but reduction above permafrost and oxidation under well-drained conditions are opposing pathways of pedogenesis. An almost constant presence of permafrost during the entire Pleniglacial and thawing during the longest GI (time-dependence), gradually leading from reducing to oxidizing conditions, could be one explanation (TG = GI model). On contrary one may assume a Pleniglacial with sporadic permafrost, especially during the coldest conditions, represented by tundra gleys (TG≠GI model; Fig. 9). Both interpretations may depend on the geographic location of the LPS studied and on the stratigraphic context.

KW2015 records a marked transition from oxidized paleosols representing GI 8 to 7 to reduced paleosols representing later GI, in agreement with Central European paleoenvironmental and global paleoclimatic records (e.g. Lisiecki and Raymo, 2005; Sirocko et al., 2016), which will be discussed in the following section. Based on chronological and stratigraphic evidence lined out above, we assume the tundra gley of unit X represents an episodic occurrence of permafrost in an overall milder MPG (TG≠GI model), related to climatic deterioration during Heinrich event 4. Fig. 10 compiles paleoenvironmental information from Willendorf and KW2015 using the TG = GI model for the cold UPG and the TG≠GI model for the milder MPG.

5.7. Implications for the Central European paleoclimatic evolution

Based on the absolute chronological information and stratigraphic reasoning, we present the paleoenvironmental information available from KW2015 (Fig. 8) on a time scale between 45 and 20 ka (Fig. 10B). Note that with increasing vertical distance from the radiocarbon ages within KW2015, chronological insecurity increases, which is indicated by lighter bars in the paleoenvironmental record. Reconstructions from the LPS Willendorf 23 km upstream the Danube (Haesaerts et al., 1996; Nigst et al., 2014) are added (Fig. 10C) with adaptions related to the paleoenvironment classes from Heiri et al. (2014).

Both loess records agree in their general stratigraphic pattern and indicate a comparable paleoenvironmental evolution. Together these LPS record millennial-scale paleoenvironmental changes from 50 to 20 ka, a period poorly reflected by other records in the Eastern Alps and their forelands (Starnberger et al., 2011; Heiri et al., 2014; Mayr et al., 2019; Moseley et al., 2020; Stojakowits et al., in press). In addition, both localities are important archeological sites and document regional environmental evolution and cultural adaption from the arrival of AMH until the LGM (Nigst et al., 2014; Staubwasser et al., 2018). A total of nine cultural layers at Willendorf are attributed to the Aurignacian (43.5–35 ka) and the Gravettian (35–29 ka); the Upper Paleolithic sequence at Krems-Wachtberg relates to the Gravettian, with an age of c. 31 ka for occupation layer AH 4.4/4.3. The regional technological change from Aurignacian to Gravettian at around 34 to 36 ka (Fig. 10C) coincides with pronounced environmental changes recorded in KW2015 as part of a general trend in climatic deterioration, along with reducing summer insolation (Fig. 10O; Berger and Loutre, 1991).

A general increase in oxygen isotope values of deep-sea foraminifera since c. 45 ka (Fig. 10M) indicates increasing global ice volume, culminating in the global LGM around 20 to 24 ka (Lisiecki and Raymo, 2005). The boundary between the milder MIS 3 to the colder MIS 2 has long seen ambiguous definitions (Sanchez Goñi and Harrison, 2010). Conventionally, the end of MIS 3 is correlated with the end of GI 3 in Greenland ice cores, which is dated to c. 27.5 ka (Andersen et al., 2006; Svensson et al., 2006). In Central European loess, the Lohne soil is identified as final paleosol of the milder MPG. Chronological constraints and regional paleoenvironmental variations lead to deviating ages for the Lohne soil and thus the MPG/UPG transition (Fig. 10D; Kadereit et al., 2013; Terhorst et al., 2015; Sauer et al., 2016). At the well-resolved and tightly dated LPS Nussloch, this boundary dates to c. 34–35 ka (Moine et al., 2017), comparable to other records from western Germany (Zens et al., 2018). Correspondingly, our evidence from KW2015 indicates the onset of the cold UPG around 34–35 ka, i.e. at the end of GI 7 (Fig. 9).

Sirocko et al. (2016) suggest the use of paleovegetation records from Eifel maar lakes as Central European reference for paleoenvironments since 60 ka, and group detailed information to landscape evolution zones (LEZ; Fig. 10L). A transition from boreal forest (LEZ 7) to steppe (with trees during interstadials; LEZ 6) around 37 ka, to tundra (LEZ 5) around 28 ka and to polar desert (LEZ 4), corresponds to overall increasingly cold conditions from 45 to 20 ka (Sirocko et al., 2016). Alpine foreland pollen records (Fig. 10E) indicate the onset of tundra vegetation at around c. 36 to 38 ka, whereas open spruce forest still predominated from 43 to 45 ka (Heiri et al., 2014 and references therein). The LPS Willendorf (Fig. 10C) records boreal conditions before 44 ka and for the following 10 ka oscillations between stadials with cold steppe/tundra ecosystems to Schwallenbach interstadials (SB Ia + b, II, III) with steppe vegetation and partly trees (Nigst et al., 2014). The two weak paleosols from KW2015 unit IX most likely correspond to SB II and III, which predate the onset of continuously cold conditions from 34 ka into the LGM.

There is remaining dispute about the onset and duration of the Alpine LGM and the timing of major glacier advances (Starnberger et al., 2011; Gaar et al., 2019). Spötl et al. (2013) report a marked environmental change from the Baumkirchen site in the Inn Valley close to Innsbruck, at around 32–33 ka, which marks the onset of the Eastern Alpine glacier advances in the Upper Würmian (UPG; Fig. 10G). First advances of the Rhine glacier into the foreland reportedly occurred around 32 ka (Fig. 10H, from a compilation by Heiri et al., 2014) or considerably later around 28 ka (Fig. 10I; Preusser et al., 2011), consistent to advances of the Garda and Tagliamento piedmont lobes in Northern Italy (Fig. 10F; Monegato et al., 2017). The MIS 2 speleothem oxygen isotope record from Siebenhengste Cave in Switzerland (Fig. 10K) supports that the maximum glaciation occurred around 24 ka (Luetscher et al., 2015), but the drivers and extents of earlier last glacial ice advances are unclear. A modelling study by Seguinot et al. (2018) suggests an early Alpine glacier advance culminating around 30 ka and a maximum advance around 24.5 ka (Fig. 10J).

Detailed chronologies for the onset and dynamics of foreland glaciations in the Danube catchment are scarce. Reuther (2007) report exposure ages of 15–17 ka from the Lake Starnberg region around (Ivy-Ochs et al., 2008), whereas Swiss perialpine lakes were ice-free at 20 ka (Fig. 10H; Heiri et al., 2014). KW2015 data indicate the presence of a polar desert representing the coldest and driest conditions around 25–23 ka, in agreement to authors that suggest LGM glacier maxima during this period (Preusser et al., 2011; Monegato et al., 2017). Chronologically robust, KW2015 indicates comparable paleoenvironmental conditions around 29–30 ka, suggesting a correspondence to earlier Alpine glacier advances, consistent with the evidence from Baumkirchen (Spötl et al., 2013), the Nesseltalgraben (Mayr et al., 2019), and the scheme from Heiri et al. (2014). Taking KW2015 reworked layers as reference, we may assume considerable Alpine glacier advances around 29–30 ka, followed by a retreat, another major advance peaking around

24–25 ka and a final moderate readvance around 20–21 ka. These fluctuations largely correspond to Ca^{2+} maxima of the NGRIP dust record (Fischer et al., 2007) and indicate a coupling to hemispheric paleoclimatic evolution with considerable support of glaciations by Heinrich events 3 and 2 and ice volume reductions during GI 4, 3, and 2.

Greenland ice cores do not clearly show the global cooling from MIS 3 to MIS 2 (Lisiecki and Raymo, 2005) but are essential references for the timing of suborbital millennial scale climatic fluctuations, i.e. Dansgaard-Oeschger (DO) and to some extent Heinrich events (Seierstad et al., 2014). Proxy variations of Alpine speleothems (Fig. 10K; Moseley et al., 2014; Moseley et al., 2020) and Central European LPS (Schirmer, 2012; Moine et al., 2017) indicate a strong link to these millennial-scale paleoclimate variations that appeared largely synchronous on a global scale (Corrick et al., 2020). Tundra gleys at Nussloch that formed between 35 and 20 ka are even larger in number than GI of the same period, which agrees to the information available from KW2015. Nussloch IG5 and KW2015 IVb have no GI analogue in the NGRIP dust and oxygen isotope records (marked with X in Figs. 9 and 10A + P).

By providing absolute age control for UPG tundra gleys, the chronostratigraphy of Nussloch overcomes circular arguments between climatic cause and paleosol type for the UPG in Central Europe (Moine et al., 2017; Rousseau et al., 2017a), supporting a chronological framework for detailed reconstructions from KW2015 (section 5.5). For the MPG, a TG = GI model requires further age control and regional differentiation. Recognizing a milder MPG and colder UPG for Krems/Willendorf is suggested to reconstruct stratigraphic features of last glacial LPS. Our results underline the coupled significance of local topography, regional paleoenvironment, catchment morphodynamics, and large scale paleoclimate in interpreting marked differences in local loess stratigraphies. Additional studies of spatially distributed LPS are required in order to regionalize past climate changes and to understand how local and catchment environments respond to these changes. These reconstructions require detailed stratigraphic information from field logging supported by high-resolution color and GS data and a careful use of paleoenvironmental proxies.

6. Conclusions

A robust stratigraphy for the LPS Krems-Wachtberg has been produced by detailed field observations and supported by spectrophotometric data. Color variations are sensitive to changes in pigmentation, which is mostly related to in situ pedogenesis or to sediments pigmented by pedogenesis. Designations of pedological horizons adequately capture the stratigraphic variability of the studied KW2015 section. High-resolution granulometry data differentiate aeolian dust from units affected by pedogenesis and reworking along the slope. Single parameters derived from GS, color or MS are unable to describe the formation of the profile and the paleoenvironmental evolution. Reconstructions of the interplay of dust accumulation, pedogenesis, and slope processes based on the stratigraphic log can be semi-quantitatively linked to paleoecosystems. Published luminescence ages indicate no major discontinuities and radiocarbon ages are important chronological tie points with considerably smaller errors. Chronostratigraphic interpretations strongly benefit from similarities of KW2015 to the tightly dated high-resolution MPG/UPG reference LPS of Nussloch, Germany.

The reconstructions of the forming processes of the LPS Krems-Wachtberg indicate the general climatic deterioration from MIS 3 to MIS 2 and close links to suborbital paleoclimatic variations recorded in Greenland ice core oxygen isotope and dust records. Paleosols that formed under oxidizing conditions are only present in the lower part of KW2015 and correspond to the Lohne soil at the LPS Nussloch, marking the rather abrupt end of the MPG around c. 34–35 ka. The UPG sequence is subdivided by tundra gleys indicating several short phases of climatic improvement, higher in number than GI. This confirms observations from West Central Europe, where the NGRIP dust record (Ca^{2+}) appears as more appropriate reference for characterizing the paleoclimatic oscillations during the last glacial. A characteristic deviation from Western Central Europe is the presence of reworked units that we attribute to the local prevalence of a polar desert during phases of maximum dust accumulation recorded in the NGRIP dust record and the LPS Nussloch. This deviation in local paleoenvironmental conditions likely relates to the more continental location of the study region and the upstream Eastern Alps. This study highlights the need for detailed reconstructions from LPS to regionalize paleoclimate and understand the impact of these changes to the landscape system. A detailed stratigraphy and thorough reconstructions of LPS development is prerequisite for using down-profile parameter variations as paleoenvironmental proxies.

Declaration of competing interest

The authors declare that they have no known competing financial interests or personal relationships that could have appeared to influence the work reported in this paper.

Acknowledgements

TS wishes to thank Christoph Spötl and Oliver Heiri for several fruitful discussions since the EU-COST funded INTIMATE meetings at Bludenz 2013 and Obergurgl 2013. Thanks to Roland Zech for help in the field and numerous stimulating discussions and to Heinz Veit for several thoughtful remarks. Grain size and color measurements were carried out in the context to the CRC 806 “Our way to Europe“, subproject B1 and D1. We thank the Deutsche Forschungsgemeinschaft (DFG, German Research Foundation), grant number INST 216/596–2, for funding this project (project number 57444011). We thank two anonymous reviewers for constructive feedback that helped improve our manuscript.

Appendix A. Supplementary data

Supplementary data to this article can be found online at https://doi.org/10.1016/j.quascirev.2020.106602.

References

Aitchison, J., 1986. The Statistical Analysis of Compositional Data. Chapman and Hall, London.
Allen, J.R.L., Thornley, D.M., 2004. Laser granulometry of Holocene estuarine silts: effects of hydrogen peroxide treatment. Holocene 14, 290–295.
Andersen, K.K., Svensson, A., Johnsen, S.J., Rasmussen, S.O., Bigler, M., Röthlisberger, R., Ruth, U., Siggaard-Andersen, M.-L., Steffensen, J.P., Dahl-Jensen, D., Vinther, B.M., Clausen, H.B., 2006. The Greenland Ice Core Chronology 2005, 15–42 ka. Part 1: constructing the time scale. Quat. Sci. Rev. 25, 3246–3257.
Antoine, P., Rousseau, D.D., Degeai, J.P., Moine, O., Lagroix, F., Kreutzer, S., Fuchs, M., Hatté, C., Gauthier, C., Svoboda, J., Lisá, L., 2013. High-resolution record of the environmental response to climatic variations during the Last Interglacial-Glacial cycle in Central Europe: the loess-palaeosol sequence of Dolní Věstonice (Czech Republic). Quat. Sci. Rev. 67, 17–38.
Antoine, P., Rousseau, D.D., Moine, O., Kunesch, S., Hatté, C., Lang, A., Tissoux, H., Zöller, L., 2009. Rapid and cyclic aeolian deposition during the Last Glacial in European loess: a high-resolution record from Nussloch, Germany. Quat. Sci. Rev. 28, 2955–2973.
Babek, O., Chlachula, J., Matys Grygar, T., 2011. Non-magnetic indicators of pedogenesis related to loess magnetic enhancement and depletion: examples from the Czech Republic and southern Siberia. Quat. Sci. Rev. 30, 967–979.
Barron, V., Torrent, J., 1986. Use of the Kubelka-Munk theory to study the influence of iron oxides on soil colour. J. Soil Sci. 37, 499–510.

Berger, A., Loutre, M.F., 1991. Insolation values for the climate of the last 10 million years. Quat. Sci. Rev. 10, 297–317.
Bibus, E., 1974. Abtragungs- und Bodenbildungsphasen im Rißlöß. Eiszeitalt. Ggw. 25, 166–182.
Blume, H.-P., Brümmer, G.W., Horn, R., Kandeler, E., Kögel-Knabner, I., Kretzschmar, R., Stahr, K., Wilke, B.-M., 2010. Scheffer/Schachtschabel Lehrbuch der Bodenkunde, 16 ed. Spektrum Akademischer Verlag, Heidelberg.
Brandl, M., Hauzenberger, C., Postl, W., Martinez, M.M., Filzmoser, P., Trnka, G., 2014. Radiolarite studies at krems-wachtberg (lower Austria): northern alpine versus carpathian lithic resources. Quat. Int. 351, 146–162.
Bronger, A., 1976. Zur quartären Klima- und Landschaftsentwicklung des Karpatenbeckens auf (paläo-)pedologischer und bodengeographischer Grundlage. Geographisches Institut, Universität Kiel, Kiel.
Bronger, A., 2008. Pedostratigraphical correlation of brunhes age loess-paleosol sequences in east and central asia with central Europe. Abh. Geol. Bundesanst. 62, 131–137.
Buggle, B., Hambach, U., Müller, K., Zöller, L., Marković, S.B., Glaser, B., 2014. Iron mineralogical proxies and Quaternary climate change in SE-European loess–paleosol sequences. Catena 117, 4–22.
Cilek, V., 2001. The loess deposits of the Bohemian Massif: silt provenance, palaeometeorology and loessification processes. Quat. Int. 76–77, 123–128.
Cornell, R.M., Schwertmann, U., 2003. The Iron Oxides. Structure, Properties, Reaction, Occurences and Users, 2 ed. Wiley-VCH, Weinheim.
Corrick, E.C., Drysdale, R.N., Hellstrom, J.C., Capron, E., Rasmussen, S.O., Zhang, X., Fleitmann, D., Couchoud, I., Wolff, E., 2020. Synchronous timing of abrupt climate changes during the last glacial period. Science 369, 963.
Ding, Z.L., Ranov, V., Yang, S.L., Finaev, A., Han, J.M., Wang, G.A., 2002. The loess record in southern Tajikistan and correlation with Chinese loess. Earth Planet Sci. Lett. 200, 387–400.
Einwögerer, T., Friesinger, H., Händel, M., Neugebauer-Maresch, C., Simon, U., Teschler-Nicola, M., 2006. Upper Palaeolithic infant burials. Nature 444, 285, 285.
Einwögerer, T., Händel, M., Simon, U., Masur, A., Neugebauer-Maresch, C., 2014. Upper Palaeolithic occupation in the Wachtberg area of Krems: the evidence of surveys, sections and core samples. Quat. Int. 351, 50–66.
FAO, 2006. Guidelines for Soil Description, 4 ed. Food and Agriculture Organization of the United Nations, Roma.
Fink, J., 1965. Die Subkommission für Lößstratigraphie der Internationalen Quartärvereinigung. Eiszeitalt. Ggw. 16, 264–275.
Fink, J., 1969. Les progres de l'etude des loess en Europe, La Stratigraphie des Loess d'Europe. CNRS, Paris, pp. 3–12.
Fink, J., 1976. Exkursion durch den österreichischen Teil des nördlichen Alpenvorlandes und den Donauraum zwischen Krems und der Wiener Pforte. ÖAW, Wien.
Fink, J., Kukla, G.J., 1977. Pleistocene climates in central Europe; at least 17 interglacials after the Olduvai Event. Quat. Res. 7, 363–371.
Fischer, H., Siggaard-Andersen, M.-L., Ruth, U., Röthlisberger, R., Wolff, E., 2007. Glacial/interglacial changes in mineral dust and sea-salt records in polar ice cores: sources, transport, and deposition. Rev. Geophys. 45.
Fischer, P., Hambach, U., Klasen, N., Schulte, P., Zeeden, C., Steininger, F., Lehmkuhl, F., Gerlach, R., Radtke, U., 2019. Landscape instability at the end of MIS 3 in western Central Europe: evidence from a multi proxy study on a Loess-Palaeosol-Sequence from the eastern Lower Rhine Embayment, Germany. Quat. Int. 502 (Part A), 119–136.
Fitzsimmons, K.E., Marković, S.B., Hambach, U., 2012. Pleistocene environmental dynamics recorded in the loess of the middle and lower Danube basin. Quat. Sci. Rev. 41, 104–118.
Fladerer, F.A., Salcher-Jedrasiak, T.A., Händel, M., 2014. Hearth-side bone assemblages within the 27 ka BP Krems-Wachtberg settlement: fired ribs and the mammoth bone-grease hypothesis. Quat. Int. 351, 115–133.
Frechen, M., Zander, A., Cilek, V., Ložek, V., 1999. Loess chronology of the last interglacial/glacial cycle in bohemia and moravia, Czech republic. Quat. Sci. Rev. 18, 1467–1493.
Fuchs, W., Grill, R., 1984. 38 Krems, Geologische Karte der Republik Österreich 1: 50.000. Geologische Bundesanstalt, Wien.
Gaar, D., Graf, H.R., Preusser, F., 2019. New chronological constraints on the timing of Late Pleistocene glacier advances in northern Switzerland. E&G Quaternary Science Journal 68, 53–73.
Gocke, M., Hambach, U., Eckmeier, E., Schwark, L., Zöller, L., Fuchs, M., Löscher, M., Wiesenberg, G.L.B., 2014. Introducing an improved multi-proxy approach for paleoenvironmental reconstruction of loess–paleosol archives applied on the Late Pleistocene Nussloch sequence (SW Germany). Palaeogeogr. Palaeoclimatol. Palaeoecol. 410, 300–315.
Groza, S.M., Hambach, U., Veres, D., Vulpoi, A., Händel, M., Einwögerer, T., Simon, U., Neugebauer-Maresch, C., Timar-Gabor, A., 2019. Optically stimulated luminescence ages for the Upper Palaeolithic site Krems-Wachtberg, Austria. Quat. Geochronol. 49, 242–248.
Haase, D., Fink, J., Haase, G., Ruske, R., Pécsi, M., Richter, H., Altermann, M., Jager, K.D., 2007. Loess in Europe - its spatial distribution based on a European Loess Map, scale 1 : 2,500,000. Quat. Sci. Rev. 26, 1301–1312.
Haesaerts, P., Borziac, I., Chirica, V., Damblon, F., Koulakovska, L., 2007. Cadre stratigraphique et chronologique du Gravettien en Europe centrale. Paleo - Revue d'archéologie préhistorique 19, 31–52.
Haesaerts, P., Damblon, F., Bachner, M., Trnka, G., 1996. Revised stratigraphy and chronology of the Willendorf II sequence, Lower Austria. Archaeol. Austriaca 80, 25–42.
Häggi, C., Zech, R., McIntyre, C., Zech, M., Eglinton, T.I., 2014. On the stratigraphic integrity of leaf-wax biomarkers in loess paleosols. Biogeosciences 11, 2455–2463.
Hambach, U., 2010. Palaeoclimatic and stratigraphic implications of high resolution magnetic susceptibility logging of Würmian loess at the Krems-Wachtberg Upper-Palaeolithic site. In: Neugebauer-Maresch, C., Owen, L.R. (Eds.), New Aspects of the Central and Eastern European Upper Palaeolithic - Methods, Chronology, Technology and Subsistence. Österreichische Akademie der Wissenschaften, Wien, pp. 295–304.
Hambach, U., Zeeden, C., Hark, M., Zöller, L., 2008. Magnetic dating of an upper palaeolithic cultural layer bearing loess from the krems-wachtberg site (lower Austria). Abh. Geol. Bundesanst. 62, 153–157.
Händel, M., 2017. The stratigraphy of the Gravettian sites at Krems. Quartar 64, 129–155.
Händel, M., Einwögerer, T., Simon, U., Neugebauer-Maresch, C., 2014. Krems-Wachtberg excavations 2005–12: main profiles, sampling, stratigraphy, and site formation. Quat. Int. 351, 38–49.
Heiri, O., Koinig, K.A., Spötl, C., Barrett, S., Brauer, A., Drescher-Schneider, R., Gaar, D., Ivy-Ochs, S., Kerschner, H., Luetscher, M., Moran, A., Nicolussi, K., Preusser, F., Schmidt, R., Schoeneich, P., Schwörer, C., Sprafke, T., Terhorst, B., Tinner, W., 2014. Palaeoclimate records 60–8 ka in the Austrian and Swiss Alps and their forelands. Quat. Sci. Rev. 106, 186–205.
ISO 11277, 2009. Determination of Particle Size Distribution in Mineral Soil Material – Method by Sieving and Sedimentation. International Organization for Standardization, Geneva.
ISO 13320, 2009. Particle Size Analysis - Laser Diffraction Methods. International Organization for Standardization, Geneva.
ISO 14688, 2017. Geotechnical Investigation and Testing — Identification and Classification of Soil — Part 1: Identification and Description. International Organization for Standardization, Geneva.
IUSS Working Group WRB, 2014. World Reference Base for Soil Resources 2014. International Soil Classification System for Naming Soils and Creating Legends for Soil Maps. FAO Roma.
Ivy-Ochs, S., Kerschner, H., Reuther, A., Preusser, F., Heine, K., Maisch, M., Kubik, P.W., Schlüchter, C., 2008. Chronology of the last glacial cycle in the European Alps. J. Quat. Sci. 23, 559–573.
Kadereit, A., Kind, C.-J., Wagner, G.A., 2013. The chronological position of the Lohne Soil in the Nussloch loess section – re-evaluation for a European loess-marker horizon. Quat. Sci. Rev. 59, 67–86.
Krauss, L., Zens, J., Zeeden, C., Schulte, P., Eckmeier, E., Lehmkuhl, F., 2016. A multi-proxy analysis of two loess-paleosol sequences in the northern harz foreland, Germany. Palaeogeogr. Palaeoclimatol. Palaeoecol. 461, 401–417.
Kukla, G.J., 1977. Pleistocene land-sea correlations I. Europe. Earth Sci. Rev. 13, 307–374.
Laj, C., Guillou, H., Kissel, C., 2014. Dynamics of the Earth magnetic field in the 10–75 kyr period comprising the Laschamp and Mono Lake excursions: new results from the French Chaîne des Puys in a global perspective. Earth Planet Sci. Lett. 387, 184–197.
Lehmkuhl, F., Zens, J., Krauss, L., Schulte, P., Kels, H., 2016. Loess-paleosol sequences at the northern European loess belt in Germany: distribution, geomorphology and stratigraphy. Quat. Sci. Rev. 153, 11–30.
Lisiecki, L.E., Raymo, M.E., 2005. A Pliocene-Pleistocene stack of 57 globally distributed benthic $\delta^{18}O$ records. Paleoceanography 20, PA1003.
Lomax, J., Fuchs, M., Preusser, F., Fiebig, M., 2014. Luminescence based loess chronostratigraphy of the Upper Palaeolithic site Krems-Wachtberg, Austria. Quat. Int. 351, 88–97.
Luetscher, M., Boch, R., Sodemann, H., Spotl, C., Cheng, H., Edwards, R.L., Frisia, S., Hof, F., Muller, W., 2015. North atlantic storm track changes during the last glacial maximum recorded by alpine speleothems. Nat. Commun. 6, 6344.
Lukić, T., Basarin, B., Buggle, B., Marković, S.B., Tomović, V.M., Popov Raljić, J., Hrnjak, I., Timar-Gabor, A., Hambach, U., Gavrilov, M.B., 2014. A joined rock magnetic and colorimetric perspective on the Late Pleistocene climate of Orlovat loess site (Northern Serbia). Quat. Int. 334–335, 179–188.
Mayr, C., Stojakowits, P., Lempe, B., Blaauw, M., Diersche, V., Grohganz, M., Correa, M.L., Ohlendorf, C., Reimer, P., Zolitschka, B., 2019. High-resolution geochemical record of environmental changes during MIS 3 from the northern Alps (Nesseltalgraben, Germany). Quat. Sci. Rev. 218, 122–136.
Meszner, S., Kreutzer, S., Fuchs, M., Faust, D., 2013. Late Pleistocene landscape dynamics in Saxony, Germany: paleoenvironmental reconstruction using loess-paleosol sequences. Quat. Int. 296, 94–107.
Meyer-Heintze, S., Sprafke, T., Schulte, P., Terhorst, B., Lomax, J., Fuchs, M., Lehmkuhl, F., Neugebauer-Maresch, C., Einwögerer, T., Händel, M., Simon, U., Solís Castillo, B., 2018. The MIS 3/2 transition in a new loess profile at Krems-Wachtberg East – a multi-methodological approach. Quat. Int. 464, 370–385.
Moine, O., Antoine, P., Hatte, C., Landais, A., Mathieu, J., Prud'homme, C., Rousseau, D.D., 2017. The impact of Last Glacial climate variability in west-European loess revealed by radiocarbon dating of fossil earthworm granules. Proc. Natl. Acad. Sci. U. S. A 114, 6209–6214.
Monegato, G., Scardia, G., Hajdas, I., Rizzini, F., Piccin, A., 2017. The Alpine LGM in the boreal ice-sheets game. Sci. Rep. 7, 2078.
Moseley, G.E., Spötl, C., Brandstätter, S., Erhardt, T., Luetscher, M., Edwards, R.L., 2020. NALPS19: sub-orbital-scale climate variability recorded in northern Alpine speleothems during the last glacial period. Clim. Past 16, 29–50.
Moseley, G.E., Spötl, C., Svensson, A., Cheng, H., Brandstätter, S., Edwards, R.L., 2014.

Multi-speleothem record reveals tightly coupled climate between central Europe and Greenland during Marine Isotope Stage 3. Geology 42, 1043–1046.
Neugebauer-Maresch, C., 2008. Krems-Hundssteig – Mammutjägerlager der Eiszeit. Ein Nutzungsareal paläolithischer Jäger- und Sammler(innen) vor 41.000–27.000 Jahren, Mitteilungen der Prähistorischen Kommission. ÖAW, Wien, p. 347.
Neugebauer-Maresch, C., Hambach, U., Anghelinu, M., 2014. Loess and the record of upper palaeolithic cultures in the Danube basin. In: Catto, N. (Ed.), Quaternary International, p. 230.
Nigst, P.R., Haesaerts, P., Damblon, F., Frank-Fellner, C., Mallol, C., Viola, B., Götzinger, M., Niven, L., Hublin, J.J., 2014. Early modern human settlement of Europe north of the Alps occurred 43,500 years ago in a cold steppe-type environment. Proc. Natl. Acad. Sci. U. S. A 111, 14394–14399.
NÖ-Atlas, 2015. Geografische Kartendienste der Abteilung Hydrologie und Geoinformation des Amts der niederösterreichischen Landesregierung: NÖ-Atlas. Karte: Geländehöhe (Laserscan). http://atlas.noe.gv.at/webgisatlas/init.aspx?karte=atlas_gelaendehoehe&ks=hoehenangaben. (Accessed 6 March 2015).
Nugteren, G., Vandenberghe, J., 2004. Spatial climatic variability on the Central Loess Plateau (China) as recorded by grain size for the last 250 kyr. Global Planet. Change 41, 185–206.
Özer, M., Orhan, M., Işlk, N.S., 2010. Effect of particle optical properties on size distribution of soils obtained by laser diffraction. Environ. Eng. Geosci. 16, 163–173.
Pécsi, M., 1990. Loess is not just the accumulation of dust. Quat. Int. 7–8, 1–21.
Pécsi, M., Richter, G., 1996. Löss: Herkunft - Gliederung - Landschaften. Bornträger, Berlin & Stuttgart.
Penck, A., 1903. Exkursionen in das Durchbruchtal der Wachau und die Lößlandschaft von Krems. In: IX. Internationaler Geologen-Kongreß; Führer für die Exkursionen. typ. Brüder Hollinek, Wien.
Preusser, F., Graf, H.R., Keller, O., Krayss, E., Schlüchter, C., 2011. Quaternary glaciation history of northern Switzerland. Quaternary Science Journal (E&G) 60, 282–305.
Prud'homme, C., Lecuyer, C., Antoine, P., Moine, O., Hatte, C., Fourel, F., Martineau, F., Rousseau, D.D., 2016. Palaeotemperature reconstruction during the Last Glacial from delta O-18 of earthworm calcite granules from Nussloch loess sequence, Germany. Earth Planet Sci. Lett. 442, 13–20.
Pye, K., 1995. The nature, origin and accumulation of loess. Quat. Sci. Rev. 14, 653–667.
Pye, K., Blott, S.J., 2004. Particle size analysis of sediments, soils and related particulate materials for forensic purposes using laser granulometry. Forensic Sci. Int. 144, 19–27.
Rasmussen, S.O., Andersen, K.K., Svensson, A.M., Steffensen, J.P., Vinther, B.M., Clausen, H.B., Siggaard-Andersen, M.L., Johnsen, S.J., Larsen, L.B., Dahl-Jensen, D., Bigler, M., Röthlisberger, R., Fischer, H., Goto-Azuma, K., Hansson, M.E., Ruth, U., 2006. A new Greenland ice core chronology for the last glacial termination. J. Geophys. Res. 111.
Rasmussen, S.O., Bigler, M., Blockley, S.P., Blunier, T., Buchardt, S.L., Clausen, H.B., Cvijanovic, I., Dahl-Jensen, D., Johnsen, S.J., Fischer, H., Gkinis, V., Guillevic, M., Hoek, W.Z., Lowe, J.J., Pedro, J.B., Popp, T., Seierstad, I.K., Steffensen, J.P., Svensson, A.M., Vallelonga, P., Vinther, B.M., Walker, M.J.C., Wheatley, J.J., Winstrup, M., 2014. A stratigraphic framework for abrupt climatic changes during the Last Glacial period based on three synchronized Greenland ice-core records: refining and extending the INTIMATE event stratigraphy. Quat. Sci. Rev. 106, 14–28.
Reimer, P.J., Austin, W.E.N., Bard, E., Bayliss, A., Blackwell, P.G., Bronk Ramsey, C., Butzin, M., Cheng, H., Edwards, R.L., Friedrich, M., Grootes, P.M., Guilderson, T.P., Hajdas, I., Heaton, T.J., Hogg, A.G., Hughen, K.A., Kromer, B., Manning, S.W., Muscheler, R., Palmer, J.G., Pearson, C., van der Plicht, J., Reimer, R.W., Richards, D.A., Scott, E.M., Southon, J.R., Turney, C.S.M., Wacker, L., Adolphi, F., Büntgen, U., Capano, M., Fahrni, S.M., Fogtmann-Schulz, A., Friedrich, R., Köhler, P., Kudsk, S., Miyake, F., Olsen, J., Reinig, F., Sakamoto, M., Sookdeo, A., Talamo, S., 2020. The IntCal20 northern hemisphere radiocarbon age calibration curve (0–55 cal kBP). Radiocarbon 1–33.
Reuther, A.U., 2007. Surface Exposure Dating of Glacial Deposits from the Last Glacial Cycle. Evidence from the Eastern Alps, the Bavarian Forest, the Southern Carpathians and the Altai Mountains. Borntraeger, Stuttgart.
Roberson, S., Weltje, G.J., 2014. Inter-instrument comparison of particle-size analysers. Sedimentology 61, 1157–1174.
Rousseau, D.D., Antoine, P., Hatté, C., Lang, A., Zöller, L., Fontugne, M., Ben Othman, D., Luck, J.M., Moine, O., Labonne, M., Bentaleb, I., Jolly, D., 2002. Abrupt millennial climatic changes from Nussloch (Germany) upper weichselian eolian records during the last glaciation. Quat. Sci. Rev. 21, 1577–1582.
Rousseau, D.D., Boers, N., Sima, A., Svensson, A., Bigler, M., Lagroix, F., Taylor, S., Antoine, P., 2017a. (MIS3 & 2) millennial oscillations in Greenland dust and Eurasian aeolian records - a paleosol perspective. Quat. Sci. Rev. 169, 99–113.
Rousseau, D.D., Svensson, A., Bigler, M., Sima, A., Steffensen, J.P., Boers, N., 2017b. Eurasian contribution to the last glacial dust cycle: how are loess sequences built? Clim. Past 13.
Sanchez Goñi, M.F., Harrison, S.P., 2010. Millennial-scale climate variability and vegetation changes during the Last Glacial: concepts and terminology. Quat. Sci. Rev. 29, 2823–2827.
Sauer, D., Kadereit, A., Kuhn, P., Kosel, M., Miller, C.E., Shinonaga, T., Kreutzer, S., Herrmann, L., Fleck, W., Starkovich, B.M., Stahr, K., 2016. The loess-palaeosol sequence of Datthausen, SW Germany: characteristics, chronology, and implications for the use of the Lohne Soil as a marker soil. Catena 146, 10–29.
Schirmer, W., 2000. Eine Klimakurve des Oberpleistozäns aus dem rheinischen Löss. Eiszeitalt. Ggw. 50, 25–49.
Schirmer, W., 2012. Rhine loess at schwalbenberg II - MIS 4 and 3. Quaternary Science Journal (E&G) 61, 32–47.
Schirmer, W., 2016. Late Pleistocene loess of the lower rhine. Quat. Int. 411, 44–61.
Schulte, P., Lehmkuhl, F., 2018. The difference of two laser diffraction patterns as an indicator for post-depositional grain size reduction in loess-paleosol sequences. Palaeogeogr. Palaeoclimatol. Palaeoecol. 509, 126–136.
Schulte, P., Lehmkuhl, F., Steininger, F., Loibl, D., Lockot, G., Protze, J., Fischer, P., Stauch, G., 2016. Influence of HCl pretreatment and organo-mineral complexes on laser diffraction measurement of loess-paleosol-sequences. Catena 137, 392–405.
Schulte, P., Sprafke, T., Rodrigues, L., Fitzsimmons, K.E., 2018. Are fixed grain size ratios useful proxies for loess sedimentation dynamics? Experiences from Remizovka, Kazakhstan. Aeolian Research 31, 131–140.
Seguinot, J., Ivy-Ochs, S., Jouvet, G., Huss, M., Funk, M., Preusser, F., 2018. Modelling last glacial cycle ice dynamics in the Alps. Cryosphere 12, 3265–3285.
Seierstad, I.K., Abbott, P.M., Bigler, M., Blunier, T., Bourne, A.J., Brook, E., Buchardt, S.L., Buizert, C., Clausen, H.B., Cook, E., Dahl-Jensen, D., Davies, S.M., Guillevic, M., Johnsen, S.J., Pedersen, D.S., Popp, T.J., Rasmussen, S.O., Severinghaus, J.P., Svensson, A., Vinther, B.M., 2014. Consistently dated records from the Greenland GRIP, GISP2 and NGRIP ice cores for the past 104 ka reveal regional millennial-scale $\delta^{18}O$ gradients with possible Heinrich event imprint. Quat. Sci. Rev. 106, 29–46.
Simon, U., Händel, M., Einwögerer, T., Neugebauer-Maresch, C., 2014. The archaeological record of the Gravettian open air site Krems-Wachtberg. Quat. Int. 351, 5–13.
Sirocko, F., Knapp, H., Dreher, F., Forster, M.W., Albert, J., Brunck, H., Veres, D., Dietrich, S., Zech, M., Hambach, U., Rohner, M., Rudert, S., Schwibus, K., Adams, C., Sigl, P., 2016. The ELSA-Vegetation-Stack: reconstruction of Landscape Evolution Zones (LEZ) from laminated Eifel maar sediments of the last 60,000 years. Global Planet. Change 142, 108–135.
Smalley, I.J., O'Hara-Dhand, K., Wint, J., Machalett, B., Jary, Z., Jefferson, I., 2009. Rivers and loess: the significance of long river transportation in the complex event-sequence approach to loess deposit formation. Quat. Int. 198, 7–18.
Spötl, C., Reimer, P.J., Starnberger, R., Reimer, R.W., 2013. A new radiocarbon chronology of Baumkirchen, stratotype for the onset of the Upper Wurmian in the Alps. J. Quat. Sci. 28, 552–558.
Sprafke, T., 2016. Löss in Niederösterreich - Archiv quartärer Klima- und Landschaftsveränderungen. Würzburg University Press. Würzburg. E-book version: https://opus.bibliothek.uni-wuerzburg.de/files/12778/978-3-95826-039-9_Sprafke_Tobias_OPUS_12778.pdf.
Sprafke, T., Obreht, I., 2016. Loess: rock, sediment or soil - what is missing for its definition? Quat. Int. 399, 198–207.
Sprafke, T., Terhorst, B., Peticzka, R., Thiel, C., 2013. Paudorf locus typicus (Lower Austria) revisited — the potential of the classic loess outcrop for Middle to Late Pleistocene landscape reconstructions. Quaternary Science Journal (E&G) 62, 59–72.
Sprafke, T., Thiel, C., Terhorst, B., 2014. From micromorphology to palaeoenvironment: the MIS 10 to MIS 5 record in Paudorf (Lower Austria). Catena 117, 60–72.
Starnberger, R., Rodnight, H., Spötl, C., 2011. Chronology of the last glacial maximum in the salzach palaeoglacier area (eastern Alps). J. Quat. Sci. 26, 502–510.
Staubwasser, M., Drăguşin, V., Onac, B.P., Assonov, S., Ersek, V., Hoffmann, D.L., Veres, D., 2018. Impact of climate change on the transition of Neanderthals to modern humans in Europe. Proc. Natl. Acad. Sci. Unit. States Am. 115, 9116.
Stevenson, F.J., 1982. Humus Chemistry: Genesis, Composition, Reactions. Wiley, New York.
Stojakowits, P., Mayr, C., Ivy-Ochs, S., Preusser, F., Reitner, J.M., Spötl, C., in press. Environments at the MIS 3/2 transition in the northern Alps and their foreland. Quat. Int..
Stuiver, M., Reimer, P.J., 1993. Extended 14C data base and revised CALIB 3.0 14C age calibration program. Radiocarbon 35, 215–230.
Svensson, A., Andersen, K.K., Bigler, M., Clausen, H.B., Dahl-Jensen, D., Davies, S.M., Johnsen, S.J., Muscheler, R., Rasmussen, S.O., Röthlisberger, R., Peder Steffensen, J., Vinther, B.M., 2006. The Greenland Ice Core Chronology 2005, 15–42 ka. Part 2: comparison to other records. Quat. Sci. Rev. 25, 3258–3267.
Terhorst, B., Kühn, P., Damm, B., Hambach, U., Meyer-Heintze, S., Sedov, S., 2014. Paleoenvironmental fluctuations as recorded in the loess-paleosol sequence of the Upper Paleolithic site Krems-Wachtberg. Quat. Int. 351, 67–82.
Terhorst, B., Sedov, S., Sprafke, T., Peticzka, R., Meyer-Heintze, S., Kühn, P., Solleiro Rebolledo, E., 2015. Austrian MIS 3/2 loess–palaeosol records—key sites along a west–east transect. Palaeogeogr. Palaeoclimatol. Palaeoecol. 418, 43–56.
Thiel, C., Buylaert, J.P., Murray, A.S., Terhorst, B., Hofer, I., Tsukamoto, S., Frechen, M., 2011. Luminescence dating of the Stratzing loess profile (Austria) - testing the potential of an elevated temperature post-IR IRSL protocol. Quat. Int. 234, 23–31.
Újvári, G., Kok, J.F., Varga, G., Kovács, J., 2016. The physics of wind-blown loess: implications for grain size proxy interpretations in Quaternary paleoclimate studies. Earth Sci. Rev. 154, 247–278.
Vandenberghe, J., 2013. Grain size of fine-grained windblown sediment: a powerful proxy for process identification. Earth Sci. Rev. 121, 18–30.
Vandenberghe, J., Sun, Y., Wang, X., Abels, H.A., Liu, X., 2018. Grain-size characterization of reworked fine-grained aeolian deposits. Earth Sci. Rev. 177, 43–52.
Viscarra Rossel, R.A., Minasny, B., Roudier, P., McBratney, A.B., 2006. Colour space

models for soil science. Geoderma 133, 320–337.
Vlaminck, S., Kehl, M., Lauer, T., Shahriari, A., Sharifi, J., Eckmeier, E., Lehndorff, E., Khormali, F., Frechen, M., 2016. Loess-soil sequence at toshan (northern Iran): insights into late Pleistocene climate change. Quat. Int. 399, 122–135.
Weninger, B., Jöris, O., 2008. A 14C age calibration curve for the last 60 ka: the Greenland-Hulu U/Th timescale and its impact on understanding the Middle to Upper Paleolithic transition in Western Eurasia. J. Hum. Evol. 55, 772–781.
Zech, R., Zech, M., Marković, S., Hambach, U., Huang, Y.S., 2013. Humid glacials, arid interglacials? Critical thoughts on pedogenesis and paleoclimate based on multi-proxy analyses of the loess–paleosol sequence Crvenka, Northern Serbia. Palaeogeogr. Palaeoclimatol. Palaeoecol. 387, 165–175.
Zeeden, C., Kels, H., Hambach, U., Schulte, P., Protze, J., Eckmeier, E., Markovic, S.B., Klasen, N., Lehmkuhl, F., 2016. Three climatic cycles recorded in a loess-palaeosol sequence at Semlac (Romania) - implications for dust accumulation in south-eastern Europe. Quat. Sci. Rev. 154, 130–142.
Zens, J., Schulte, P., Klasen, N., Krauß, L., Pirson, S., Burow, C., Brill, D., Eckmeier, E., Kels, H., Zeeden, C., Spagna, P., Lehmkuhl, F., 2018. OSL chronologies of paleo-environmental dynamics recorded by loess-paleosol sequences from Europe: case studies from the Rhine-Meuse area and the Neckar Basin. Palaeogeogr. Palaeoclimatol. Palaeoecol. 509, 105–125.
Zöller, L., Richter, D., Blanchard, H., Einwögerer, T., Händel, M., Neugebauer-Maresch, C., 2014. Our oldest children: age constraints for the Krems-Wachtberg site obtained from various thermoluminescence dating approaches. Quat. Int. 351, 83–87.